國立臺灣大學理學院物理學系

碩士論文

Department of Physics
College of Science
National Taiwan University
Master Thesis

# 可提供光譜分析的細胞級解析度眼底鏡

# A subcellular-resolution spectro-ophthalmoscope

游鈞彥

Jiun-Yann Yu

指導教授：朱士維 博士

Advisor: Shi-Wei Chu, Ph.D.

中華民國 98 年七月

July, 2009



國立臺灣大學 物理所 碩士論文 可提供光譜分析的細胞級解析度眼底鏡 游鈞彥 撰 97 2

# 國立臺灣大學碩士學位論文

# 口試委員會審定書

## 可提供光譜分析的細胞級解析度眼底鏡
## A subcellular-resolution spectro-ophthalmoscope

本論文係游鈞彥君（r96222041）在國立臺灣大學物理所完成之碩士學位論文，於民國九十八年七月二日承下列考試委員審查通過及口試及格，特此證明

口試委員：

（簽名）

（指導教授）

# 致謝

能完成這篇文章，與其說我沒有放棄努力，不如說這世界還沒放棄我。時間退回兩年半，民國九十六年的春節前夕，也是碩士班考試前夕，我還在金六結 901 旅三營三連當個苦哈哈的教育班長。那時橋來橋去，只能擠出一個月來念書，匆匆寫完考古題就應考去了。兩個月後放榜，印象中我只比錄取分數高了三分。靠著這三分，一次驚奇而可愛的旅程就此展開。我必須感謝這過程中所有和我遭遇的人們，謝謝你們總是在關鍵的時刻伸出神來之手，才讓我能有今日的成就。

最應該感謝的是我的老師，亦是我的朋友，偶爾也是我咬牙切齒的對象的朱士維教授。感謝老師把對研究的熱誠傳染給我，以及他總是上窮碧落下黃泉的替我挑毛病，讓我學著做一個實事求是的科學人。我也要感謝實驗室的所有夥伴們，感謝你們對我的包容與幫助，以我的脾氣之差你們還願意跟我和諧相處，你們真的很不簡單。特別要感謝廖寶貝每每被我揶揄但並沒有懷恨在心(還是其實是有的？)；謝謝鄭岳弘提供我穩定的光源，並且勇敢的接下了這套系統；謝謝我的老同學翰軒在還沒有薪水可領的時候就從關渡跑來解救我這電路白癡；謝謝宗衍激起我罰球的準度。另外，還要感謝即將拿到博士學位的貞翰學長，您真是光學的活字典，實驗的小叮噹，讓我用最快的速度習得新知，預祝您研究之路一帆風順。

我要深深的感謝四個人，金工廠的吳新波吳師傅，系上的黃智穎黃助教，台科大的林淵祥教授和他的學生國手徐小強同學(預祝小強今年能獲得大獎，為台灣爭光)。他們總是在百忙之中，不計辛勞的提供我幫助，且不願收取任何形式的酬勞。我無法想像沒有吳師傅替我加工的器材，黃助教借用的儀器，還有林教授和徐同學替我們製作的高難度電路，我的整個系統會長成什麼支離破碎的樣子。

還要感謝應電實驗室的陳志宇助教借用訊號產生器，隔壁實驗室的陳威廷學長借用游標尺、脈衝產生器，凝態中心張玉明教授借用光纖平移台，史賓納科技林承學經理借用影像擷取卡，我的老朋友李建中和張祐豪借用高速偵測器和直流電源供應器，還有 Daniel Côté 教授在影像擷取上提供的諮詢及建議。當然，一定要感謝 University of Bath 的 Jim Stone 博士和 Jonathan Knight 教授提供他們神奇的光子晶體光纖，讓我的系統增色許多。

感謝台大電機系孫啟光教授，陽明生醫光電所高甫仁所長擔任我的口試委員，謝謝你們對後輩指導不遺餘力，讓我重新認識了自己的研究內容。感謝系辦公室的季力偉先生總是不厭其煩提醒我該注意的行政程序，我也感謝全體系辦人員在行政事務上所提供的協助。讓我也自以為的感謝一下吳俊霖先生，China Blue 全體團員，楊乃文女士以及動力火車全體團員，感謝他們的音樂支持我度過好幾個深夜與清晨。

還需另闢段落來表達我的敬意的，是香廚早餐的周秋鴻周老闆，新亞洲儀器的蕭樹森蕭經理和弘惠光電的黃佳緯黃業務工程師，除了周老闆提供我營養而廉價的早餐，蕭經理給我

擷取卡上的諮詢，以及黃工程師協助的採購之外，我在他們身上學到的，是對自己的工作的熱情與尊重。他們總是努力提供自己最好的服務，他們是我督促自己努力的榜樣，如果說我對自己有一點期許的話，我希望自己能像他們一樣，做一個尊重自己的工作，用心提供他人的服務的人。

最後，我感謝我的祖母與外祖母，我的父親與母親及我的姊姊，雖然我在這段時間總是忽略了你們，也幾乎不讓你們知道我在忙些什麼，但你們的支持從不間斷。我要感謝我的老朋友林彥超總是在我低落之時提供各式怪力亂神的解釋，讓我總能即時得到慰藉。謝謝文萱，謝謝你這麼長一段時間的陪伴、容忍、鼓勵與不吝批評。

以上，是這篇論文能發表所不可或缺的人們。我的致謝並不足以榮耀他們，因此，我只能用最慎重的態度撰寫我的碩士論文，希望能不要辜負他們對我的付出與期待。

# 摘要

眼底鏡對眼科醫師而言，就像聽診器對外科醫師一樣重要。這兩個儀器有一個共通的特性：不必透過血淋淋的解剖就能得到極有價值的資訊。然而直到上世紀末，也就是在荷姆霍茲(Hermann von Helmholtz)發明它的兩百多年之後，隨著雷射掃描顯微術與適應性光學元件的蓬勃發展，此儀器的光學設計才有重大的演進。

近年來的適應性光學雷射掃描眼底鏡正是一個顯著的例子。它大體上繼承了共軛焦雷射掃描顯微術的架構，但因為應用上的所遭遇的問題，仍需要許多修改。主要的問題在於從眼底反射回來的光強度太弱，相較之下掃描系統中的透鏡所產生的表面反射會造成相對明亮的背景。在這篇論文裡，我們將發表一個僅由面鏡架構而成的適應性光學雷射掃描眼底鏡。當我們以球面鏡取代凸透鏡，可以有效解決表面反射的問題。但球面鏡架構並不是一個完美的解決方案，它會造成斜向入射像差。本文將分析球面鏡架構的斜向入射像差，並提出一個特殊的幾何設計來補償這種像差。只有面鏡的適應性光學雷射掃描眼底鏡有另一發展潛力：在寬頻的光源/光訊號上的應用。將寬頻雷射光源導入這個系統，可提供光譜解析度極高的影像資訊。

我們的眼底鏡的性能經過光學程式的模擬及最佳化之後，在整個掃描範圍之內，都能達到繞射極限的標準。文中將描述它的架構方式，並說明如何將系統的密實度、光路架設的可行性以及系統性能全部納入考慮。透過波前及光譜的測量，我們將展示在光波長 550 nm 至 750 nm 之間，這個系統達到繞射極限的能力。

# Abstract

The significance of an ophthalmoscope to an oculist is as that of a stethoscope to a cardiologist, because these instruments collect valuable information without things going into bloody anatomy. Nevertheless, after Hermann von Helmholtz invented his ophthalmoscope in 1851, there was no major improvement of its optical design until the booming era of laser scanning microscopy and adaptive optics in the late twentieth century.

Though the adaptive optics scanning laser ophthalmoscope (AOSLO) inherits the concept of confocal laser scanning microscopy (CLSM), modifications should be done to suit its application. The main issue is that the extremely weak signal, due to the low reflectivity of the retina, would suffer from a relatively bright background scattered back from the surfaces of convex lenses of the scanning system. In this thesis, a spectro-ophthalmoscope with mirror-based scanning system and adaptive optics system is demonstrated, mainly to replace all the convex lenses with spherical mirrors. The disadvantage of mirror-based systems, the off-axis aberration, is illustrated and analyzed. We propose a specific geometrical design to compensate this aberration. With only mirrors in our spectro-ophthalmoscope, broadband capability can be achieved by choosing appropriate metallic coatings. Coupled with a broadband laser source the possibility of obtaining high-spectral-resolution information is provided.

The performance of our spectro-ophthalmoscope is simulated and optimized using optical design software. Through the optimization the diffraction-limited performance is achieved within the entire scanning area. The physical construction of this system is presented, and the compactness, optics alignment and performance of the system are all taken into considerations. With wavefront measurements, we demonstrate the diffraction-limited performance of this system from 550-nm to 750-nm wavelength.

# 目　錄

# Contents

# Chapter I Introduction

To say the inventor of the ophthalmoscope is a physicist would be just out of my arrogance of physics, because this inventor is also recognized as a talented physiologist and mathematician, as much as a pianist and an enthusiastic mountain climber, and that is Hermann von Helmholtz [1]. If we compare his ophthalmoscope, which should be an antique nowadays, with a "modern" one that our oculists usually hold in their hands, we can see that the major improvement is in the human factor rather than the optical design of this tool [2].

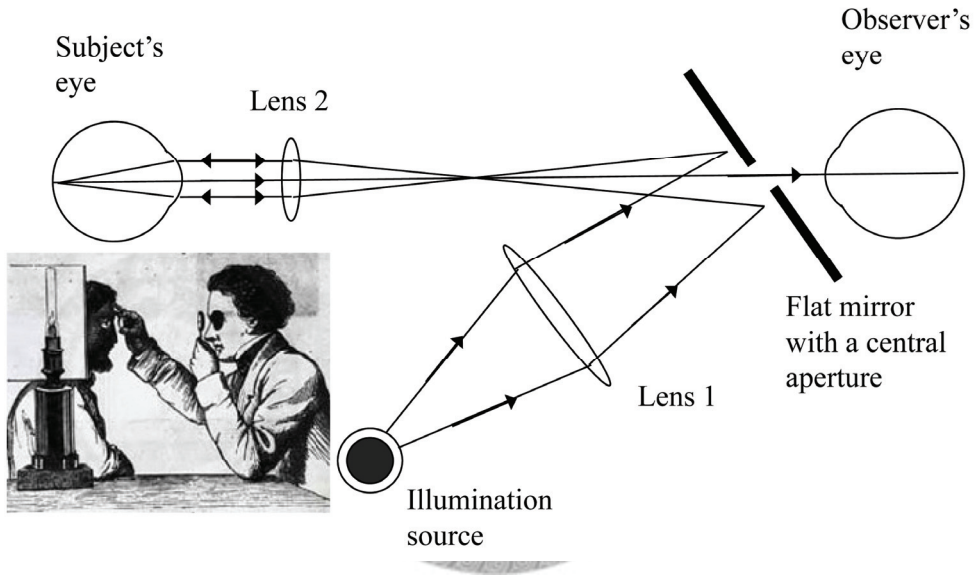


Figure 1.1 Helmholtz's ophthalmoscope. In the inset candle light is used as the illumination source and Lens 1 of the scheme is omitted [3].

The first revolution of the ophthalmoscope design took place in 1980, more than 200 years after Helmholtz's invention. Webb et al. transferred the concept of confocal microscopy to build their scanning laser ophthalmoscope (SLO) [4]. Equipped with the photomultiplier this new ophthalmoscope achieves much higher sensitivity of the retinal imaging than that of photographic films, and thus provides the possibilities of real-time retinal video. With the help of a pinhole to block the light from out-of-focus plane, optical sectioning is also realized.

However, SLO cannot achieve higher lateral resolution than traditional ophthalmoscopes,

because it still suffers from the strong aberration induced by the cornea (and sometimes even the lens) of the eye. Though it has been calculated that the aid of appropriate confocal pinhole would improved the lateral resolution by a factor of approximately 1.4 [5], under strong high-order aberrations this factor is of no significance. By measuring this aberration with a Shack-Hartmann wavefront sensor, Miller et al. simulated the corresponding point spread function and obtained retinal images with cellular resolution through de-convolution. Yet their method succeeded only for optically excellent eyes, while the cone mosaic still seemed quite blurred in general cases [6]. More recently, Liang et al. combined their custom-built Shack-Hartmann wavefront sensor with a commercial 37-actuator deformable mirror to construct a close-loop adaptive optics system, and demonstrated to the world that their subcellular-resolution retinal images can be obtained from general eyes [7].

Liang's close-loop adaptive optics has been widely adopted for various applications in ophthalmological imaging systems from then on. Roorda et al. integrated this adaptive optics system into a SLO and demonstrated the first AOSLO [8]. This combination of the advantages of SLO and high-resolution retinal imaging provided many potential applications to ophthalmology and such as the disease diagnostics, micro surgery on the retina and ultra-high-precision eye tracking [9-11].

Hyper-spectral imaging is another objective to be expected in the next-generation ophthalmoscopes. It has been known that from spectral information we can obtain molecular contrast without complicated staining processes which may even be deleterious for *in-vivo* applications. Our retinas naturally bear profound spectral information due to its design for color vision. With *in-vivo* observations of the spectral information on the retina, great improvement will be made for our understanding of the function of color vision [12,13].

Methods of spectro-ophthalmoscope developed in the last five years were mainly based on switching color filters in front of a broadband source or adopting two or more laser sources in a system [7,12,14]. These approaches increase the complexity of the optical system yet provide a very limited number of the spectral bands. In this thesis I will focus on how to modify an AOSLO design to equip it with hyper-spectral imaging capability with up to 40 spectral bands within the visible regime, which offers wavelength flexibility and spectral resolution adequate for biomedical and psychological studies. With our innovative design, it is possible to collect the hyper-spectral images in real-time.

In chapter II I will introduce the brief histories as well as mechanisms of the main components of my spectro-ophthalmoscope. Most of details of the optical design are analytically described and numerically simulated in chap. III. I will demonstrate that this system is in itself diffraction-limited

without the aid of adaptive optics or any other correction devices. Practical constructions and experimental confirmations of my spectro-ophthalmoscope will be given in chap IV and V respectively. In the future we will utilize this spectro-ophthalmoscope to study the degeneracy of color vision of deep sea fishes before we activate it into human vision study.

# Chapter II Backgrounds of an AOSLO

## II.1 Overview

For an AOSLO, as in fig. 2.1.1, there should be at least one light source which generates EM waves to interact with the object of observation, a scanning system to transform the fixed light source into a scanning beam, and then some detection devices to collect the signal and display the images. The adaptive optics, which seems unnecessary for imaging formation, is actually a revolution to ophthalmoscopes. This device, providing a similar yet better function as our spectacles, helps us correct the optically imperfect eyes and thus enhance the resolution of the image to subcellular level.

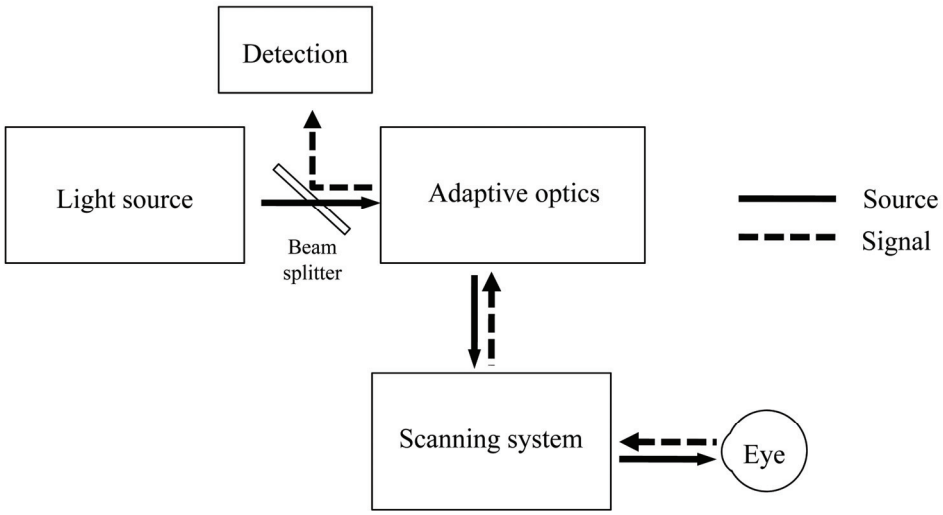


Figure 2.1.1 The scheme of an AOSLO.

## II.2 Diffraction-limited performance

Since we are talking about a high-resolution imaging system, we should first certify the meaning of "high-resolution." Through the theory of EM waves it has been known that the resolution of an far-field imaging system is ultimately limited by diffraction. Practically, diffraction limit can be defined in several aspects. The Strehl ratio is a simple criterion which describes the complicated behavior of the point spread function (PSF) in an aberrated system by only one value [15]. This ratio is equal to the reduced intensity of the peak point of the aberrated system referenced to an ideal aberration-free system, as fig. 2.2.1. Normally a system with Strehl ratio higher than 0.8 is considered diffraction-limited. Another aspect, the Marechál criterion defines the diffraction limit as a root-mean-square (rms) wavefront error less than 1/14 wavelength. The definition of rms wavefront error is illustrated in fig. 2.2.2 that,

$$\text{rms wavefront error} = \frac{1}{A}\int_{\text{The area}} (z(r,\theta) - \bar{z})^2 \, da \qquad \text{Eq. 2.2.1(a)}$$

while

$$\bar{z} = \frac{1}{A}\int_{\text{The area}} z(r,\theta) da \qquad \text{Eq. 3.1.1(b)}$$

These two criteria are both deduced from the Rayleigh criterion, and are in fact only equivalent to it under the consideration that spherical aberration is the only source of the aberration in the optical system. Nevertheless they are still good approximation under complicated superposition of aberrations [15]. Therefore, we can simulate the PSF and wavefront map at the focal plane of the objective, as fig. 3.1.4, to compare our system with the 0.8-Strehl-ratio, the Marechál criterion and the Rayleigh criterion to determine how far we are away from being perfect. In the whole design of our system, the aberration is always our first consideration.

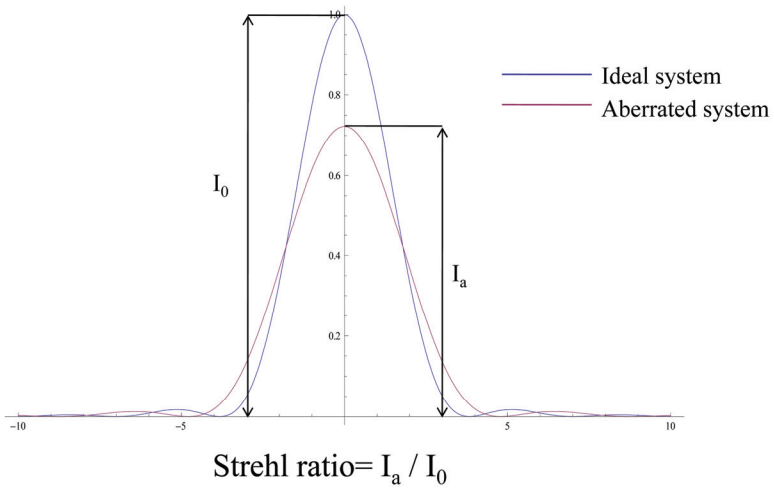


Figure 2.2.1 The Strehl ratio.

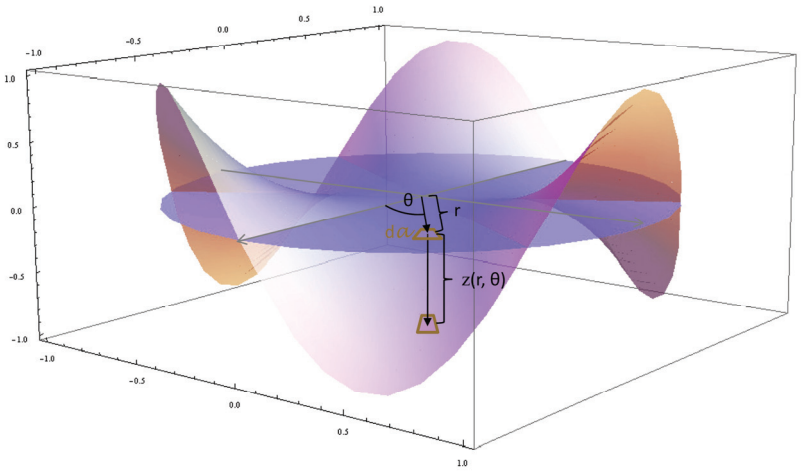


Figure 2.2.2 An aberrated wavefront.

To analyze the aberration in an optical system, Frist Zernike, the inventor of phase contrast microscope and the Nobel laureate rewarded for this invention, had developed a set of orthonormal 2-dimension polynomials to describe the wavefront map. This analysis is extremely useful to identify the types of aberrations in various kinds of imaging systems and facilitate the system correction. Lots of terms we use to describe the defect of an optical system, such as defocus and astigmatism, are in fact evolved from this set of polynomials. Table 3.2.1 is the first few terms of Zernike polynomials and their corresponding expressions [16].

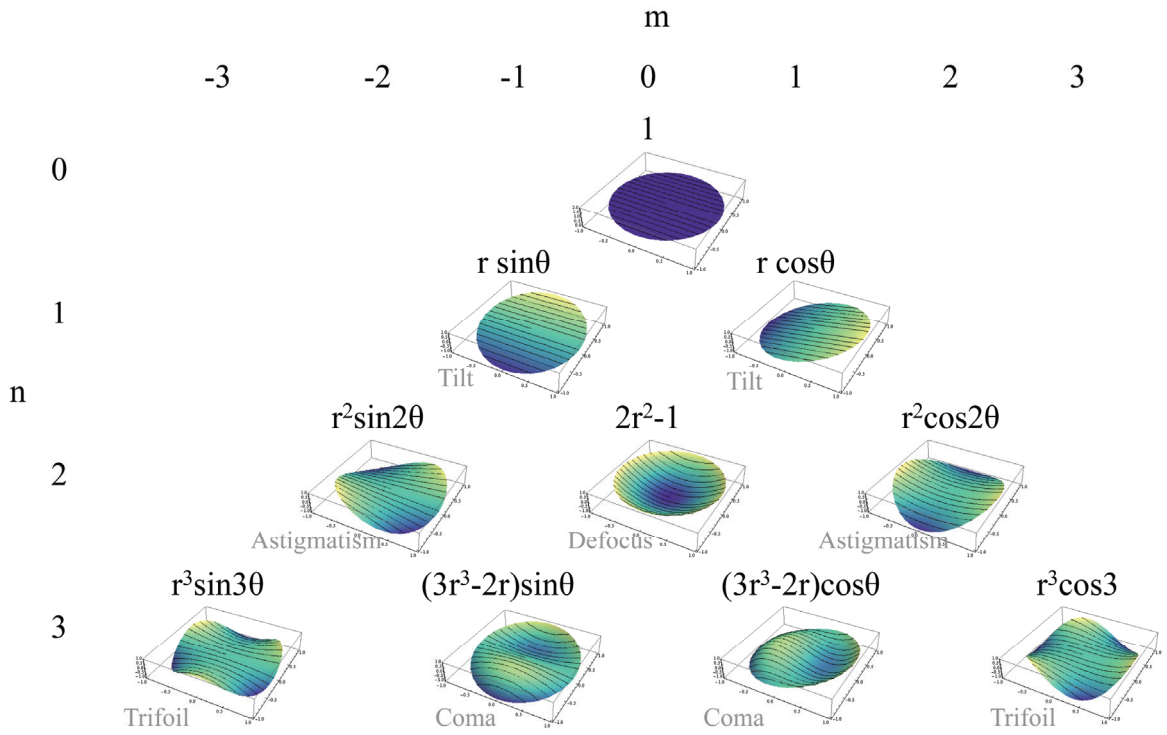


Table 2.2.1 Several low-order terms of Zernike polynomials, $Z_n^m$.

## II.3 The light source

From fig. 1.1.1 we see that at Helmholtz's time, candle light is used as the light source, and after two hundred years, people have replaced it with various lamps. Then, in the first scanning laser ophthalmoscope Webb adopted an $Ar^+$ laser (514-nm wavelength) after spatial filtering as the light source [4], and Roorda coupled a diode laser into a single-mode optical fiber to achieve even better

beam mode and wavefront flatness for high resolution imaging[8]. Both of these two ophthalmoscopes require precise alignment for the light source, therefore modification of the light source is quite inconvenient. Liang's ophthalmoscope, sometimes called a fundus camera, used a flash lamp for illumination [7]. Beam mode and wavefront flatness of the source are not so critical in this type of applications because they attempt to illuminate the whole area of interest with each single flash. Though the light source of Liang's ophthalmoscope can be easily modified to suit specific purpose, in his scheme there is hardly possibility for optical sectioning and other advantages of SLO as we mentioned in Chap. I.

In order to acquire the spectral information without complicate combination of various laser sources and losing optical sectioning ability, we adopted the supercontinuum generation, using a photonic crystal fiber (PCF) coupled with an ultra-fast laser source [17], as our light source. This supercontinuum generation provides a broadband light source starting from ultra-violet, through visible, to near-infrared regime. With such a broad bandwidth, adequate spectral information can be expected, and new possibilities of experiment design for vision studies are also provided.

The supercontinuum is not the only candidate of broadband light source, and in fact we have considered the xenon arc lamp for its easier setup compared with coupling the pump laser into the photonic crystal fiber. However we observed that the beam profile of the lamp is far from any regular or symmetrical distribution and mode filtering is extremely necessary. As a result of the irregular mode of the xenon lamp this mode filtering would give us tremendous power loss, and this inevitable tradeoff shows the other advantage of supercontinuum generation over the xenon arc lamp. The PCF we use is in itself a single-mode fiber with its core around 5 μm in diameter, and thus the generated supercontinuum is easy to be modified as a collimated Gaussian beam without chromatic aberration by using a parabolic mirror.

## II.4 Scanning system

Before we look into my scanning system we should first review some important works about confocal microscopy, the fundamental concept which this system is constructed with.

As Prof. James Pawley remarked in the preface of *The Hand Book of Biological Confocal Microscopy*, confocal microscopy is a good idea that was invented, forgotten, and then reinvented. This idea was brought forward to the world in 1957 by Marvin Minsky, a postdoctoral fellow at Harvard University then. Fig. 2.4.1 is Minsky's confocal microscope applied for patent in 1957[18].

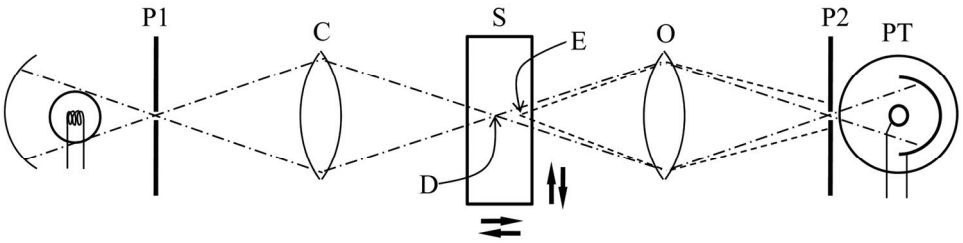


Figure 2.4.1 Minsky's confocal scanning microscope. The condenser lens C projects the point-like source from the first pinhole P1 onto a thick specimen S, and the objective lens O projects the scattered light from the specimen onto the second pinhole P2. The first pinhole is conjugated with the point D and the second pinhole. Another point, such as E in the specimen, would be less illuminated because the light source mainly focuses on D, and furthermore, most of light scattered from it would not pass the second pinhole. Therefore, the light reaching the phototube P from E is greatly attenuated compared with that from D. In Minsky's design the scanning is performed by two orthogonally vibrating tuning forks supporting the specimen stage, driven by electromagnets at 60 and 6,000 Hz.

This fantastic idea had not had a stage equal to its insight into biomedical applications until the late seventies, when computers and lasers became affordable to scientists. Soon in 1985, six papers from four separate research groups independently demonstrated the unusual capability of this new technique to reduce blurring of the image in thick light-scattering objects, and therefore three-dimensional information can be obtained through non-invasive optical sectioning [19-24].

Based on the scheme in fig. 2.4.1 it is clear that the capability of optical sectioning would depend on the size of the detector, or the pinhole. To derive this function of optical sectioning theoretically we will consider a uniformly illuminated plane as the object, and calculate the averaged intensity falling on a circular-aperture detector along the optical path, as in fig. 2.4.2(a). If we have an ideal single point detector, under the paraxial approximation, the axial intensity I distribution along the optical path is derived as [5]:

$$I(u) = \left(\frac{\sin u/2}{u/2}\right)^2 \qquad \text{Eq. 2.4.1}$$

While u is related to real axial distance z, that

$$u = \frac{8\pi z}{\lambda}\sin^2\left(\frac{\alpha}{2}\right) \qquad \text{Eq. 2.4.2}$$

where $\lambda$ is the wavelength. In fig. 2.4.2 (b) eq. 2.4.1 is plotted to illustrate the effect of optical sectioning, showing an axial resolution of

$$\frac{\lambda}{4\sin^2\frac{\alpha}{2}} \approx \frac{\lambda}{NA^2} \qquad \text{Eq. 2.4.3}$$

Here NA denotes the numerical aperture of the lens. Further calculations for finite-size pinhole would show that this sectioning ability is insensitive to pinhole radius up to $r_d/3.77$, while $r_d$ is referred to the Airy radius at the image plane [25].

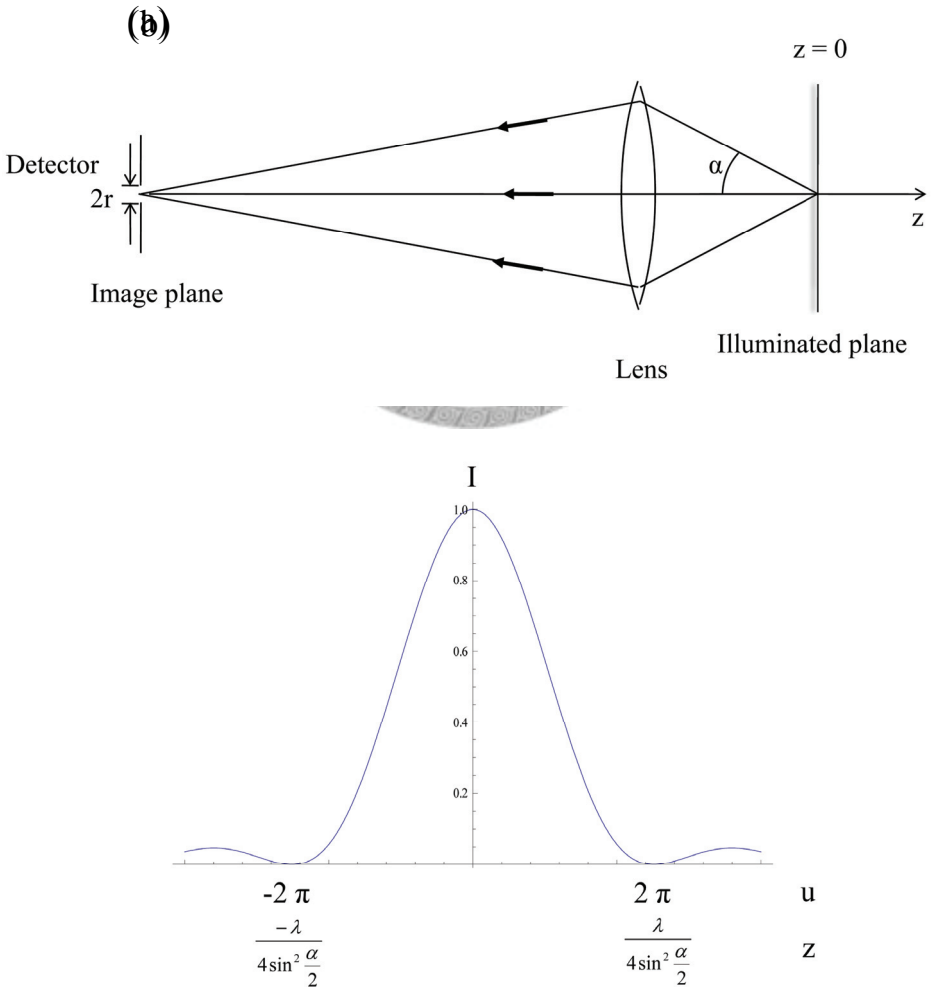


Figure 2.4.2 On-axis intensity distribution.

A major issue for Minsky's design is that the scanning is performed through vibrating the specimen in a high frequency, usually several KHz, a method not feasible for most of in-vivo observations. Nowadays most scanning laser microscopy adopt scanning mirrors, usually called scanners, to delineate scanning pattern on a fixed specimen.The scanner we use here is actually a flat mirror tilting along a specific axis, and intuitively we can find that with only a scanner we are not able to perform scanning because the beam enters the pupil only within a very small angle, as fig. 2.4.3(a), and therefore we need some other optical design to confine the scanning beam to the pupil. A telescope is an ideal solution for this application, with the scanner and pupil being correctly placed in conjugation, as in fig. 2.4.4.

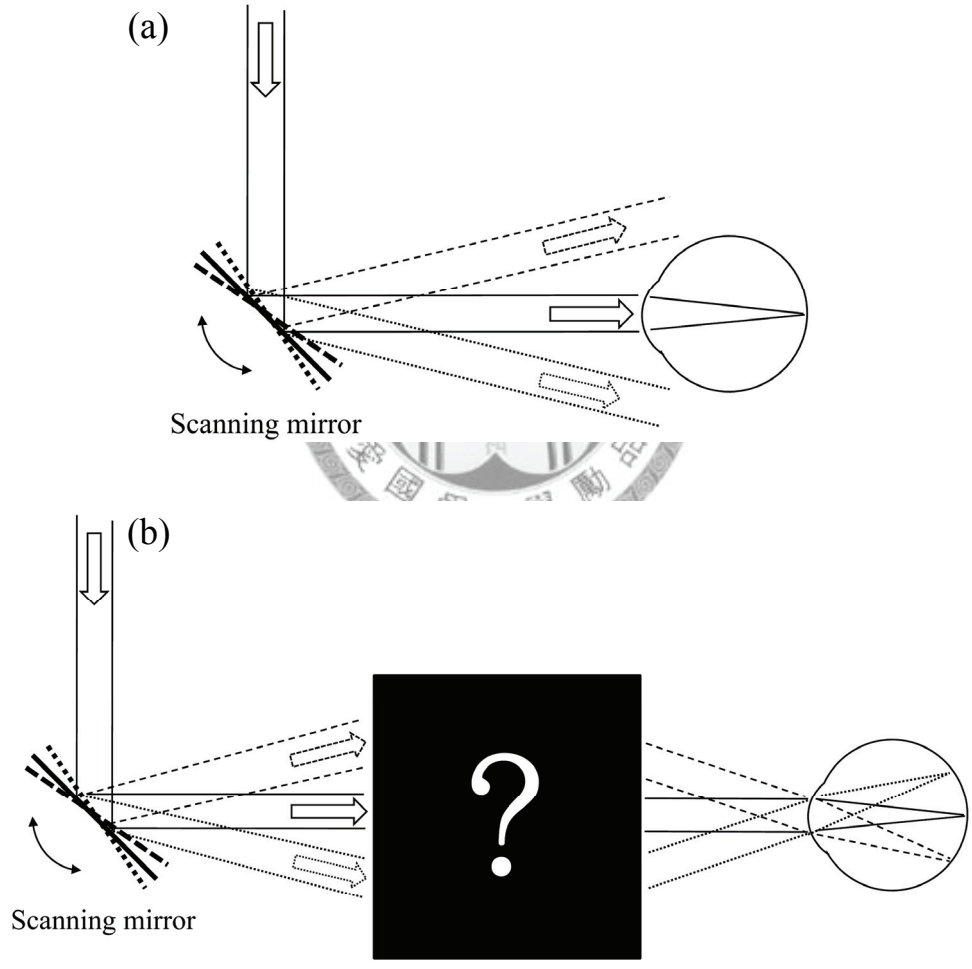


Figure 2.4.3 Projection of the scanning beam.

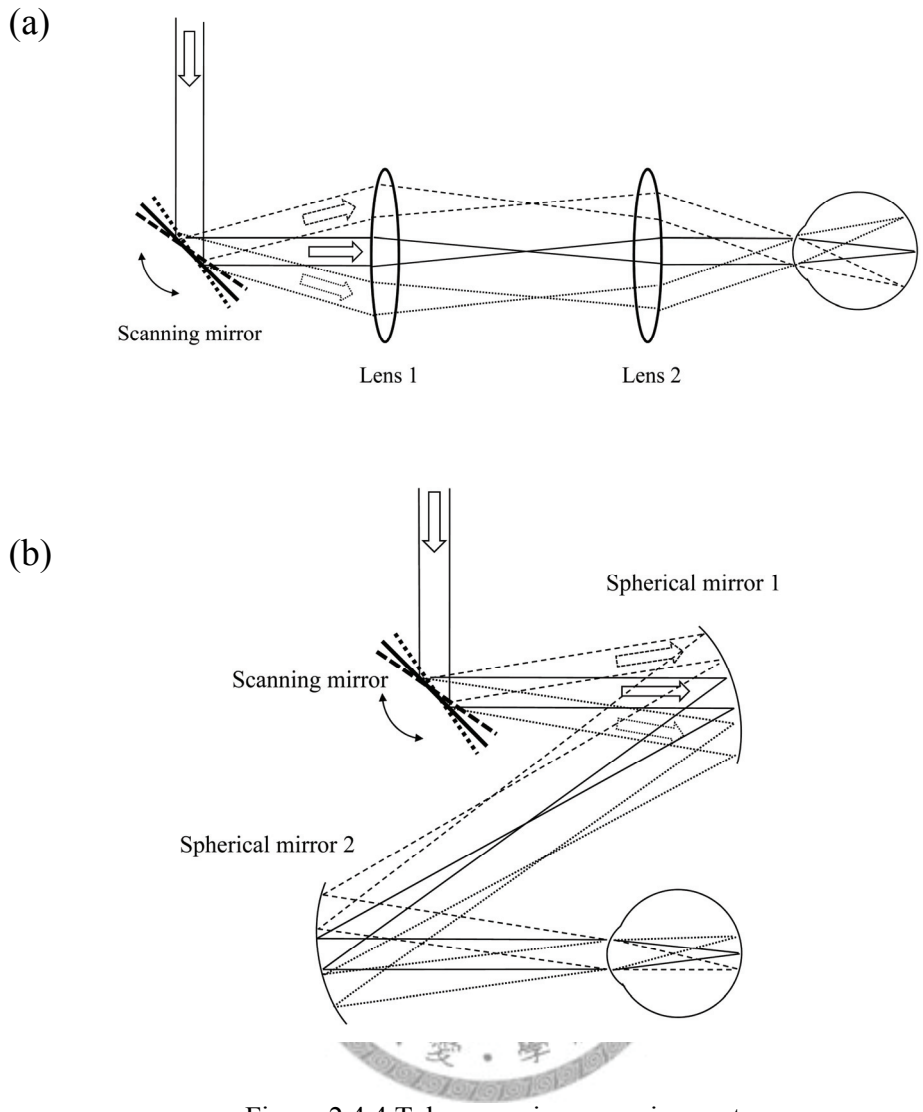


Figure 2.4.4 Telescopes in a scanning system.

As to relay the scanning beam, a telescope consists of concave mirrors can work as well as the one consists of converging lenses, and mirror-based telescopes have some significant advantages in ophthalmology. The first and the most important advantage is that lenses produce ghost reflections but mirrors don't. To image the retina in-vivo, what we can collect is only the light scattered back to the optical system, which is relatively weak compared with our light source due to the low reflectivity of our retinas, typically around 5 %, and only 1 % of this reflected light exits the pupil. Under this circumstance the ghost reflection will be extremely harmful to the contrast of the image. Though we can always choose antireflection coating on lens surfaces for desirable wavelength, these coatings still allows about 1 % reflection, which is one-order above the scale of the signal from the retina, and this reflection adds up for all the lenses in the optical system.

Figure 2.4.5 Images with different contrast. A white background is added to the image on the right hand side, and thus lower the contrast.

Another disadvantage of lens-based telescopes is the chromatic aberration, which is not as critical as ghost reflection but requires additional adjustment of the system after the laser source being tuned to a different wavelength.

As illustrated in fig. 2.4.4(b), mirror-based telescope requires off-axis incidence on mirrors, which brings much complication in alignment of these optics. Complicated alignment can be accomplished by hard working, yet off-axis incidence induces more troubles than that, the off-axis aberrations. Details about this issue are discussed later in Chap. III.

## II.5 Adaptive optics

Coincidently, adaptive optics shares similar fate with the confocal microscopy. Horace Babcock suggested in 1953 that through a close-looped compensation of wavefront error induced by atmospheric turbulence, there would be considerable improvement in performance for large ground-based astronomical telescopes [26]. However, not until twenty years later had Hardy and his colleagues demonstrated the first real-time adaptive optics system at frequency in the kilohertz range [27]. With the improvement in computer technology in the 1990s adaptive optics systems began to be adopted for many major ground-based telescopes, which now even achieve images with higher resolution than those obtained with the Hubble space telescope [28].

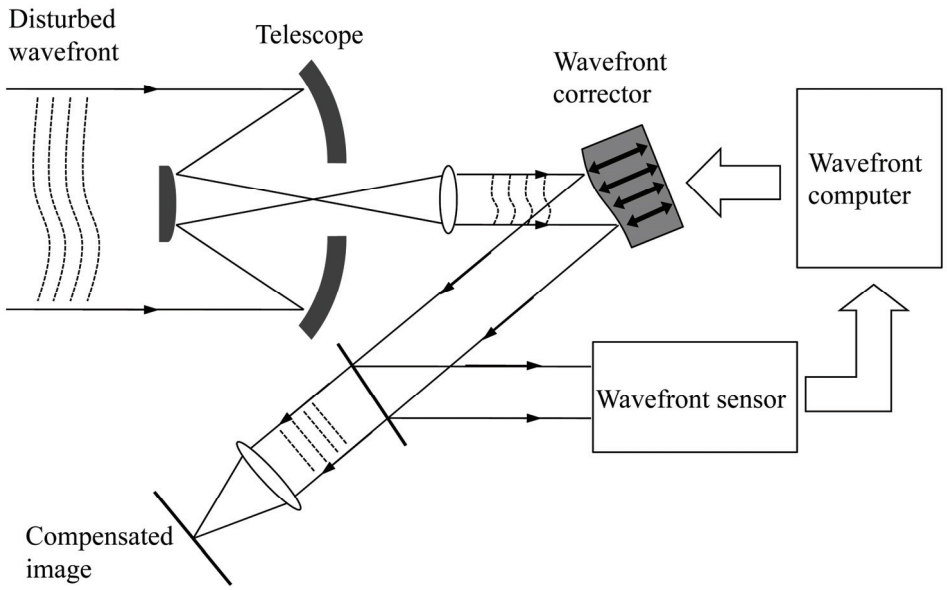


Figure 2.5.1 Simplified scheme of Hardy's close-loop adaptive optics. The wavefront is measured by wavefront sensor and reconstructed by the computer. After the reconstruction the computer output the corresponding correction to the wavefront corrector, which is a deformable mirror driven by many small actuators.

The capability of image enhancement of adaptive optics soon aroused the attention of researchers in ophthalmology, because wavefront error induced by irregular cornea has been known as the main issue for both poor vision and dissatisfying resolution of retinal image. In 1997, Liang et al. published the first ophthalmoscope based on a close-looped adaptive optics system capable of high-order-aberration correction, along with convincing subcellular-resolution retinal images [7]. Several types of wavefront sensors had been developed for measuring ocular aberrations since 1950s. They were based on subjective ray tracing, the Foucault test and modified aberroscopes [29-31]. However, these methods either require lengthy calculations, complicated design, or provide analysis for only low-order aberrations, which means they are not ready for clinical applications. This situation changed when Liang demonstrated that it was possible to adopt Shack-Hartmann wavefront sensor to measure the ocular aberrations [32]. This wavefront sensor with lens array is a modified Hartmann test in which local slopes of a wavefront is tested.

There is a slightly different function of adaptive optics between the Hardy's design and the AOSLO. The adaptive optics is not only set to correct the signal but also pre-correct the source. Fig. 2.5.2 illustrates that to minimize the focal spot on the retina, the source should be pre-corrected to

compensate the wavefront distortion of the cornea. The relation between the focal spot and the aberration will be described in III.3. Details of arrangement of the adaptive optics will be given in IV.4.

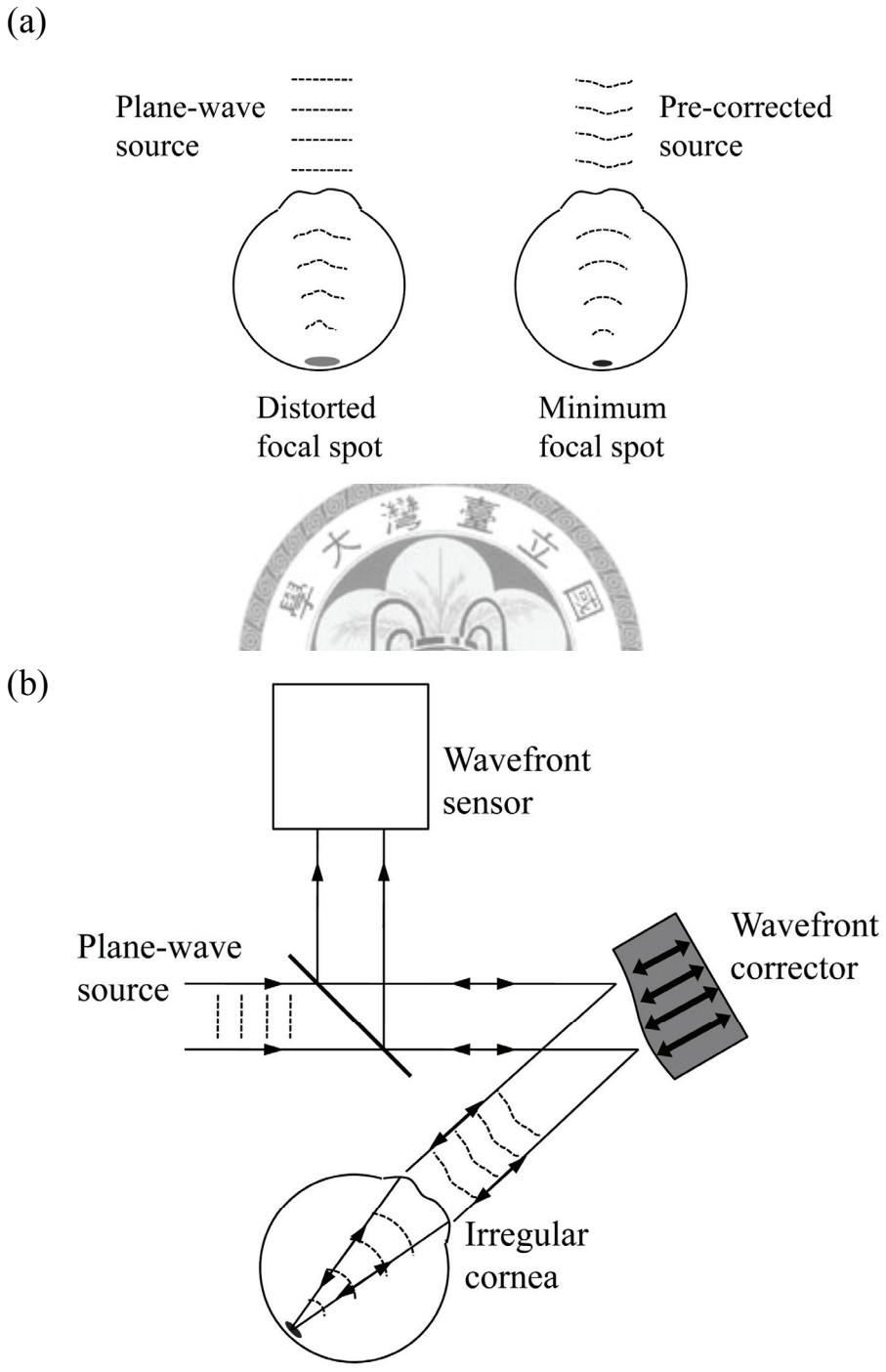


Figure 2.5.2 Schematic of the function of adaptive optics in a retinal imaging system.

## II.6 Digital image formation

One of the natures of the scanning mechanism is that spatial information of the object would be transferred into temporally sequential data. We used a photomultiplier tube to collect this data, for its extreme sensitivity to photons. To plot the image out of these sequential data requires dramatic technical efforts, and fortunately, similar techniques have been developed long time ago for our daily-life technology, the TVs. In fact since the 1990s various image-processing techniques, of both hardware and software, have been invented to suit specific purposes of different kinds of confocal microscopy [18]. Nevertheless, we still rely on a TV-related technique, the frame grabber, for its readiness of high speed processing.

Frame grabbers are by themselves developed for high-frame-rate and real time video acquisition, and thus make the AOSLOs suitable for clinical applications. Another advantage of the high frame rate is that the short acquisition time prevents the image blurring due to eye movement, which is a complicated oscillation of around 10 Hz in frequency [33]. Details of synchronization between the scanning system and the frame grabber would be presented in IV.5.

# Chapter III Optical design: optimization of the scanning system

## III.1 Off-axis aberrations

We have discussed the advantages of mirror-based telescopes while applied to the laser scanning microscopy (LSM) in chap. II.3, nevertheless, most LSM, no matter commercial or custom-built systems, adopt lens-based telescopes in their scanning system. In addition that lens-based telescope makes the alignment easier, a more critical issue is that, the aberrations introduced by oblique incidence on spherical mirrors deteriorate the resolution of the entire imaging system significantly.

Fig. 3.1.1 shows the design of our first-generation mirror-based scanning system in our laboratory. In this design we adopt long-focus spherical mirrors in order to reduce both the angle of oblique incidence and f-number (beam diameter / focus) on spherical mirrors of the scanning system.

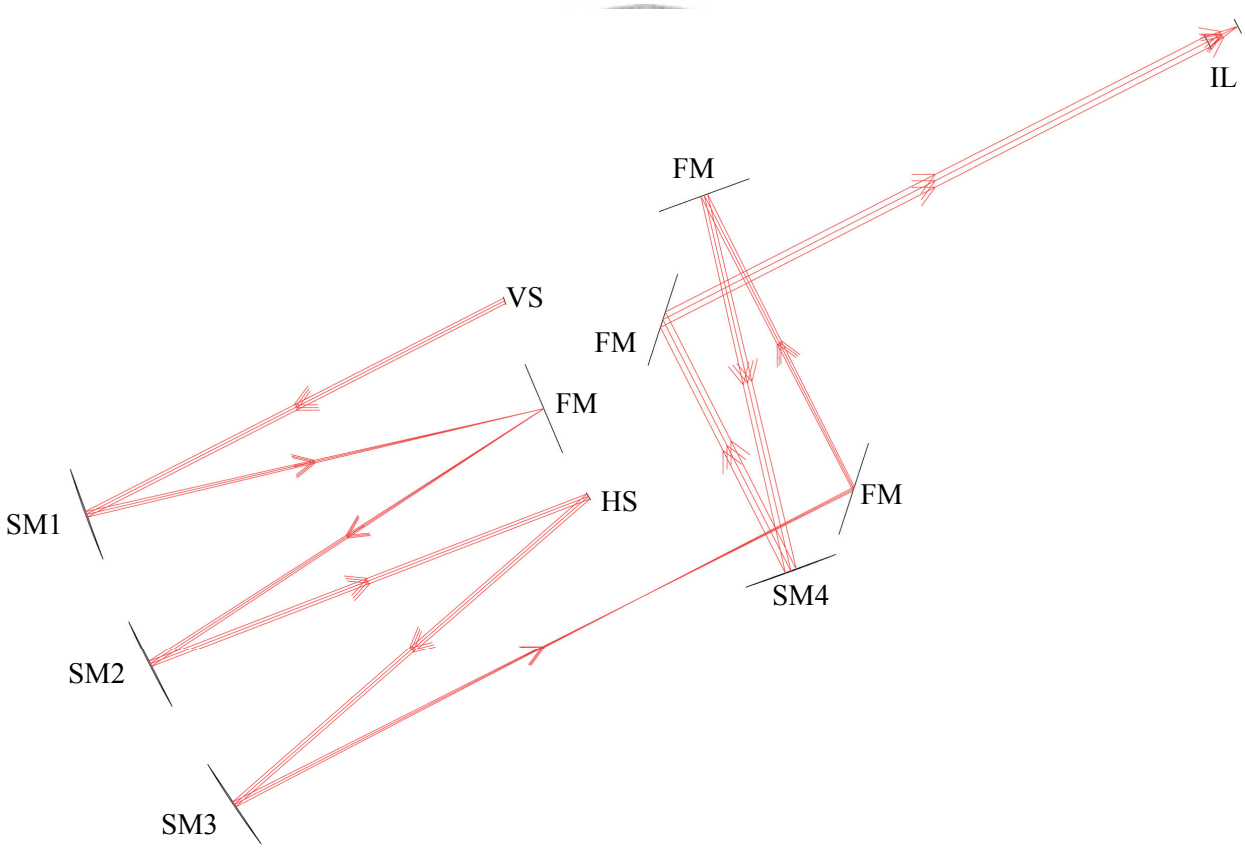


Figure 3.1.1 Our first-generation mirror-based scanning system. VS, vertical scanner; HS, horizontal scanner; SM1-3, spherical mirrors with 500-mm radius of curvature; SM4, spherical mirror with 1000-mm radius of curvature; FM: flat mirror; IL: ideal lens with 18-mm focus.

Here we simulate the system performance through an optical design program ZEMAX. The objective of the microscope is set as an ideal thin lens in simulation so that we can identify the aberrations only from the scanning system.

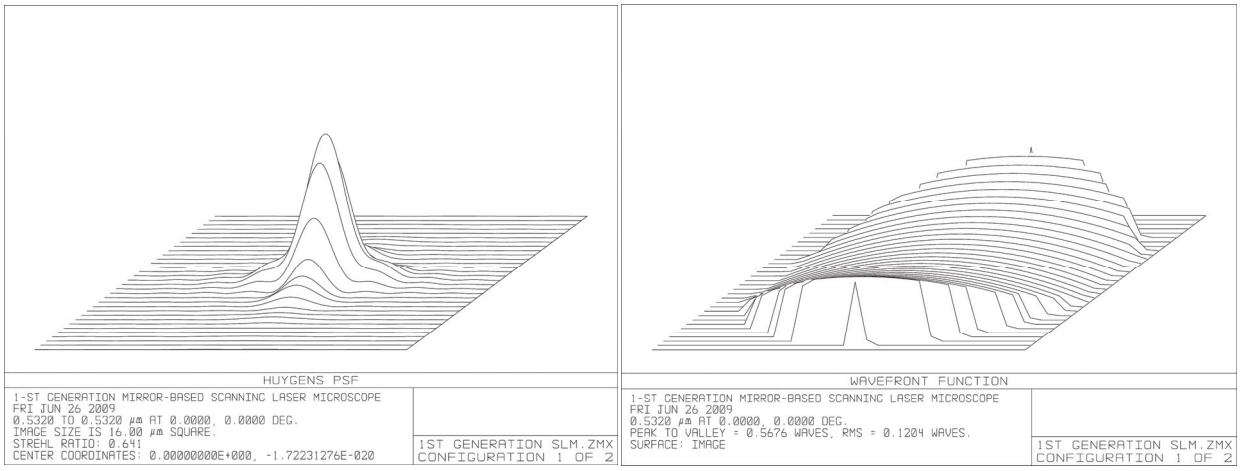


Figure 3.1.2 Simulations of our first-generation mirror-based scanning system, at the center of the scanning area. The corresponding Strehl ratio is 0.641; rms wavefront error, 0.12 wave; wavelength: 532 nm.

The wavefront map in fig. 3.1.2 can be expanded in Zernike polynomials,

$$-0.0001\,Z_2^0 - 0.1223\,Z_2^2 - 0.0004\,Z_3^{-1} + O(10^{-5}) \qquad \text{Eq. 3.1.1}$$

and from table 2.2.1 we can identify the off-axis alignment results in significant astigmatism and slight coma.

## III.2 Compensation of astigmatism and coma

Eq. 3.1.1 tells us that the wavefront error is mostly contributed by astigmatism, so let us focus on its compensation with more discussion. As a matter of fact, astigmatism is usually the only concerned aberration in current scanning systems for AOSLO [8, 33]. The residual coma, which is at least

one-order smaller than astigmatism, is considered to be ignorable compared with the aberration induce by the cornea.

Astigmatism can be compensated by different approaches if we start from different questions: what is it? Or how is it introduced by a spherical mirror? To answer the first question we can simply find the expression of astigmatism in Zernike polynomials, and the plot of it shows inverse curvatures along two orthogonal axes, as in table 2.2.1. Therefore, to compensate astigmatism, we need a correction optics exhibiting different optical power along these two axes, as illustrated in fig. 3.2.1. Besides that a cylindrical lens turns out to be straightforward solution [8], laser cavity designers have also found a Brewster-cut crystal useful to astigmatism correction for a focusing beam [34].

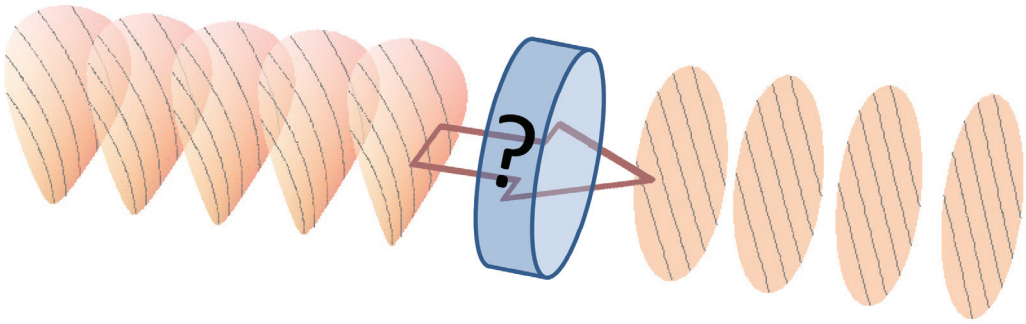


Figure 3.2.1 Compensation of astigmatism.

To answer the second question, we should define sagittal and tangential plane before further discussion. For an oblique incidence the definition of tangential plane is identical to plane of reflection (considering the chief ray only), and the plane containing orthogonal to the tangential plane would be sagittal plane, as shown in fig. 3.2.2.

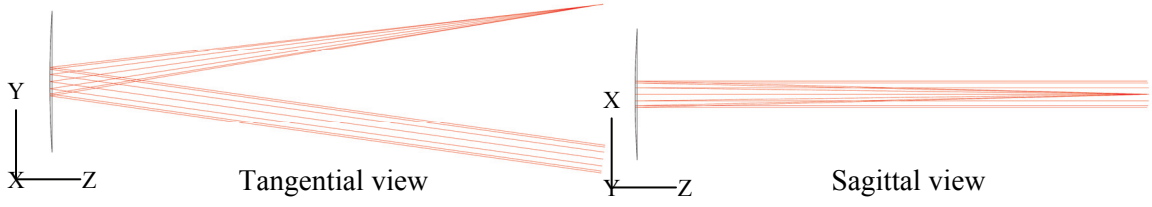


Figure 3.2.2 Off-axis incidence on a spherical mirror. Radius of curvature of the spherical mirror: 200 mm, beam diameter: 5 mm, incident angle: 8° .

Spherical mirrors are known for half-radius focus in normal incidence case under paraxial approximation, but in off-axis case, tangential beam and sagittal beam in fact “experience” different focal lengths [34]. Instead of complicated geometry and derivations, here I simply present the simulation results of through-focus spot diagram of the scheme in fig. 3.2.3, which shows the slight difference between the focal lengths of these two planes. This difference in focal lengths adds astigmatism to our scanning system. Besides that the focal point is about 1.5 times larger than the airy diameter in the dimensions of our setup, astigmatism also significantly elongates the depth of focus. These two phenomena would result in lower lateral resolution and axial resolution.

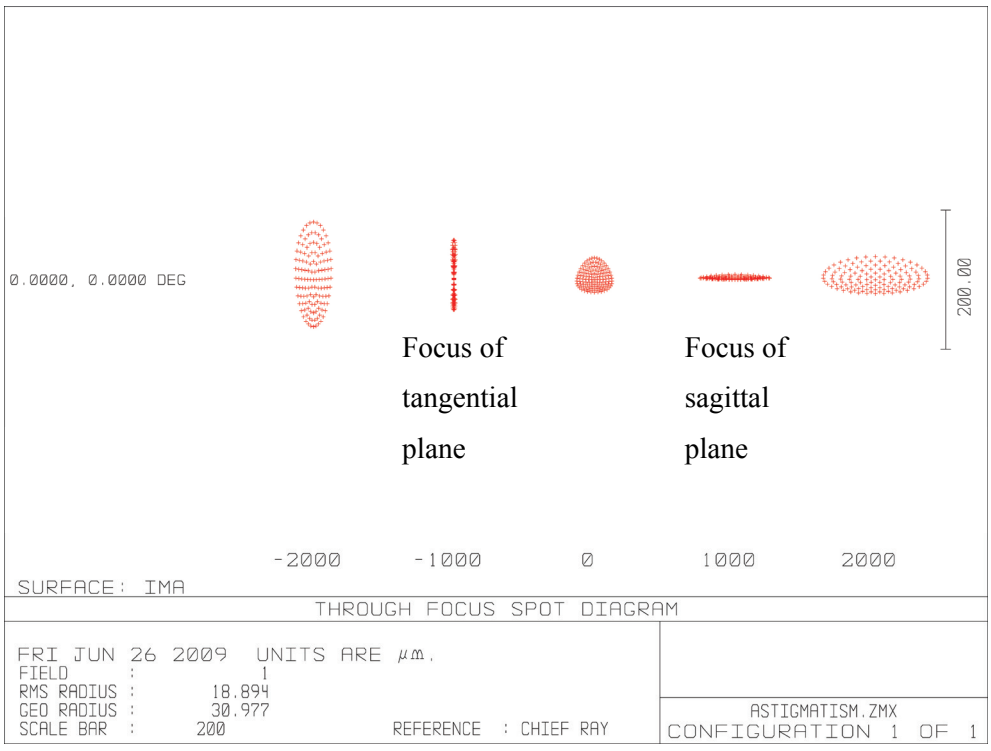


Figure 3.2.3 The astigmatism induced by oblique incidence in fig. 3.2.2. The radius of curvature of this mirror is 200 mm and the beam diameter is 5 mm.

Since Maxwell’s equations are by themselves time-reversible, we can consider about this problem of astigmatism backward. As in fig. 3.2.4., the time reversal of our case is, interestingly, that astigmatism is removed after the reflection by a spherical surface. Therefore, the strategy of astigmatism compensation is simply to find out the form of astigmatism on the surface of the

second spherical mirror of the telescope and tilt this mirror along a specific axis, which would be easily proved to be orthogonal to the axis of tilt of the first spherical mirror. I use an ideal lens Obj, as shown in fig. 3.2.5, to demonstrate this geometrical compensation design.

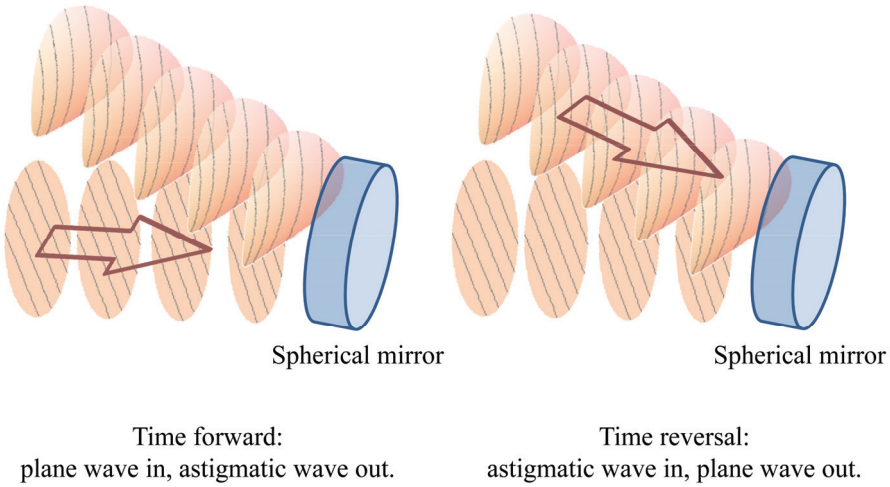


Figure 3.2.4 Oblique incidence on a spherical mirror.

Now we can play the same time-reversal trick on coma compensation. However, due to the geometrical properties of coma and astigmatism we found that the axis of tilt for coma compensation is perpendicular to the one for astigmatism compensation. All the compensation design are illustrated and simulated in fig. 3.2.5. Note that the astigmatism compensation design demonstrates not only greatly improved symmetry along the optical axis, but also much reduced focal spot size, which predict improvement in both axial and lateral resolution.

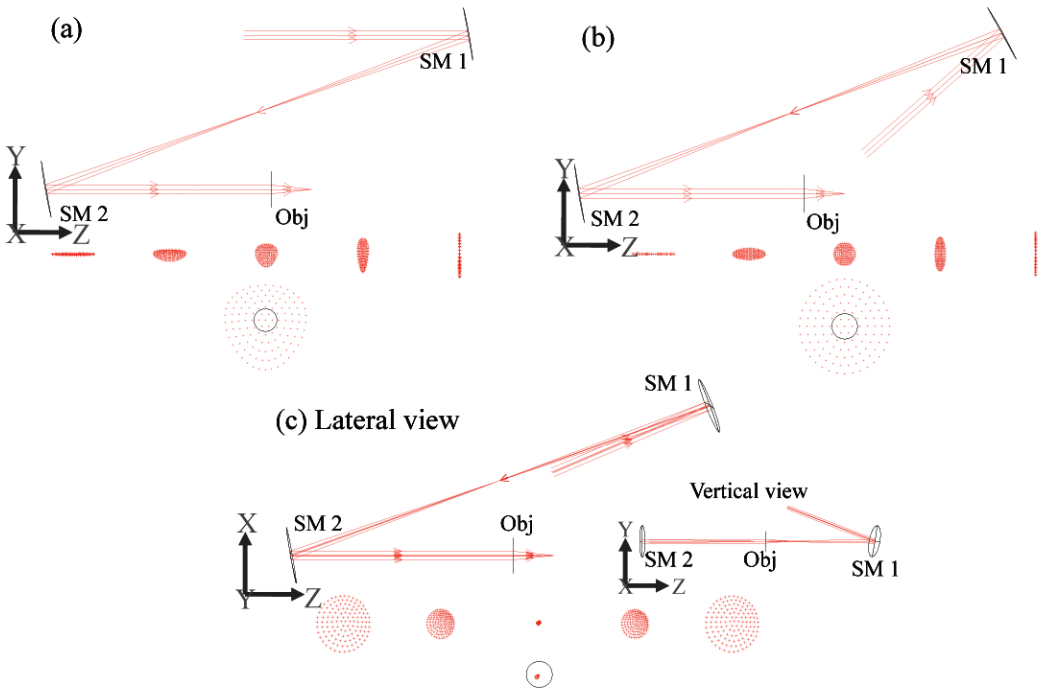


Figure 3.2.5 Schemes and simulations of (a) a typical design, (b) coma compensation design and (c) astigmatism compensation design of relaying telescopes. The spot diagrams along beam propagation direction (50 mm interval) and at focal point are shown respectively under the corresponding scheme. Scale: the circle in the spot diagram indicates the Airy disk, which is 7.8 mm in diameter. The oblique incidence is 10 degree on each spherical mirror. Note that the focal spot size in (c) is one order of magnitude smaller than that in (b). SMs: concave spherical mirror with 200-mm radius of curvature; Obj: ideal thin lens with 18-mm focal length.

Based on these two kinds of aberration compensations discussed above, the choice of the axis of tilt of the second spherical mirror determines which kind of aberrations will be compensated. This finding indicates that an off-axis incidence on the first spherical mirror induces both astigmatism and coma, but only one of them can be removed after the beam being reflected by the second spherical mirror. According to the design mentioned in II.4, there would be actually four spherical mirrors in my scanning system. Let's consider naively if we have four spherical mirrors, can we remove coma and astigmatism simultaneously by carefully choosing the axis of tilt for each mirror? Fortunately, the answer from numerical simulation is yes. With four spherical mirrors in the path, it is possible to compensate coma and astigmatism simultaneously, as the layout shown in fig. 3.2.6. The horizontal scanner (HS), vertical scanner (VS), and the back aperture of the objective are

conjugate planes to each other. In this layout the astigmatism compensation pairs are SM 1 + 2 and SM 3 + 4, while the coma compensation pairs are SM 1 + 3 and SM 2 + 4.

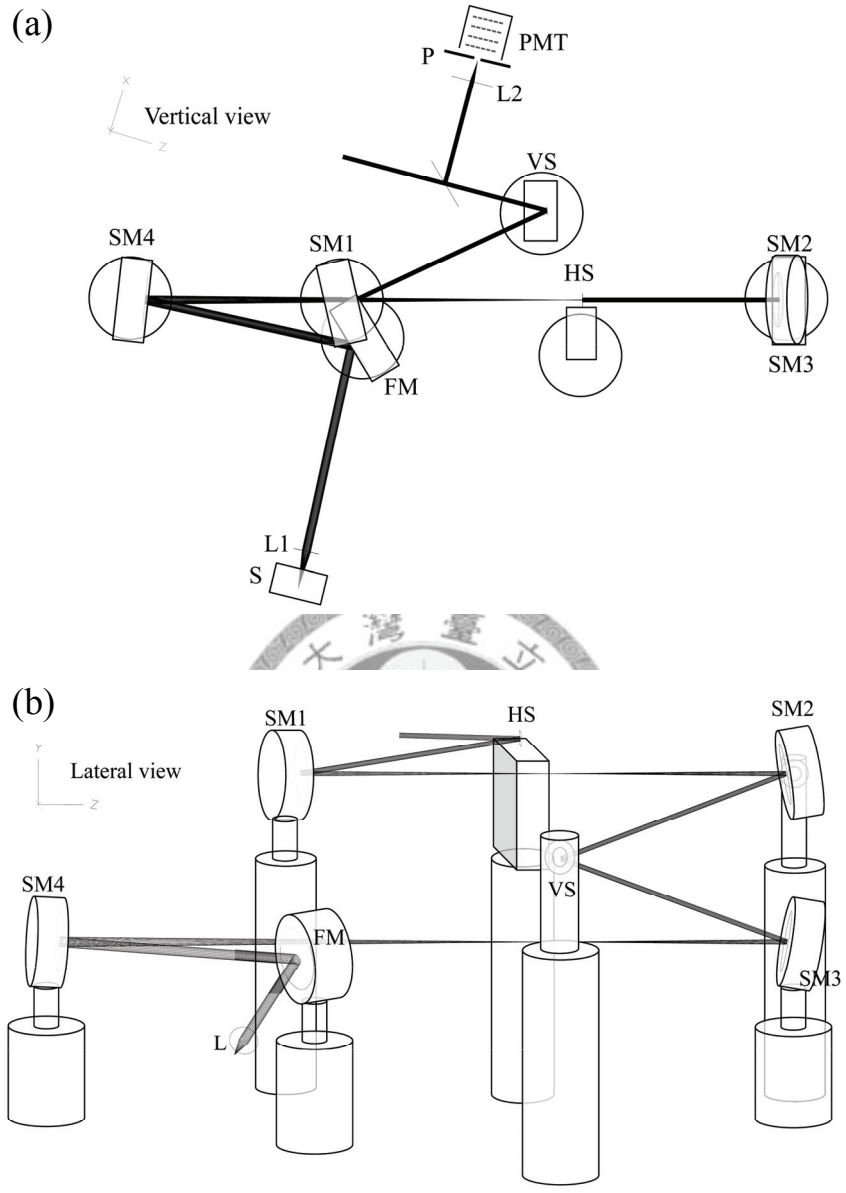


Figure 3.2.6 Mirror-based scanning system with both coma and astigmatism compensated.

As discussed in III.1, to examine the performance of the scanning system, here I present simulation results on rms wavefront error and Strehl ratio, and compare them with the wavefront measurement, as shown in fig. 3.2.7. Note that these results are only from the center of the scanning area, and therefore I further simulated the rms wavefront errors and Strehl ratios with the 4-mm beam diameter within a 3°×3° scanning range, according to the ideal lens L. See fig. 3.2.8.

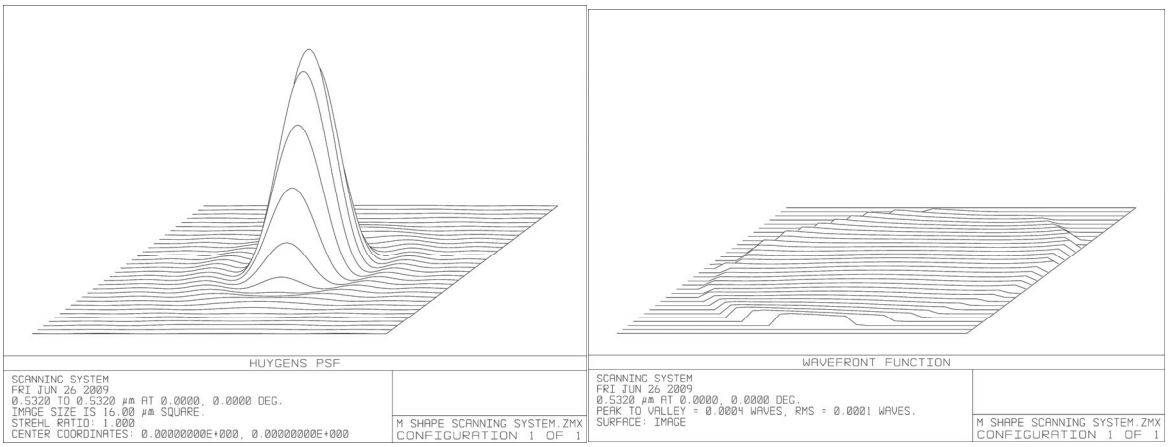


Figure 3.2.7 Simulations at the center of the scanning area of our off-axis aberration compensation design. The corresponding Strehl ratio and rms wavefront error are 1.000 and 0.0001 $\lambda$. Wavelength: 532 nm.

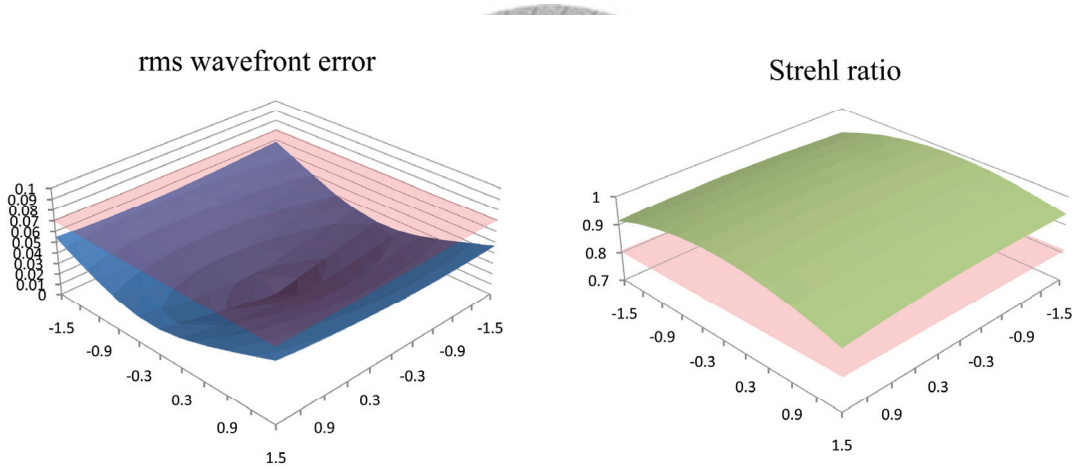


Figure 3.2.8 Simulated rms wavefront error and Strehl ratio within the scanning range. The pink planes indicate the criteria of diffraction limit, a 0.07-wave rms wavefront error and a 0.8 Strehl ratio.

In Zernike-polynomial analysis of this scanning system we found that all the coefficients belong to order of $10^{-5}$ or even lower, at the center of the scanning area. Please notice that in our first-generation scanning system we adopt a much smaller f-number design, in which higher-order aberrations are usually insignificant. Now with the geometrical compensation technique we could have a larger f-number design, in other words, the shorter radius of curvature of the spherical mirrors, to satisfy both performance and compactness.

# Chapter IV　Realization of a spectro-ophthalmoscope

In this chapter, I will first list all the devices adopted for my spectr-ophthalmoscope in the first section, and further discuss the details of these devices and constructions following this section. In figure 4.1 the laser source part is separated from the whole system for clarity. The corresponding symbol of each device can be found in the notes of the part lists.

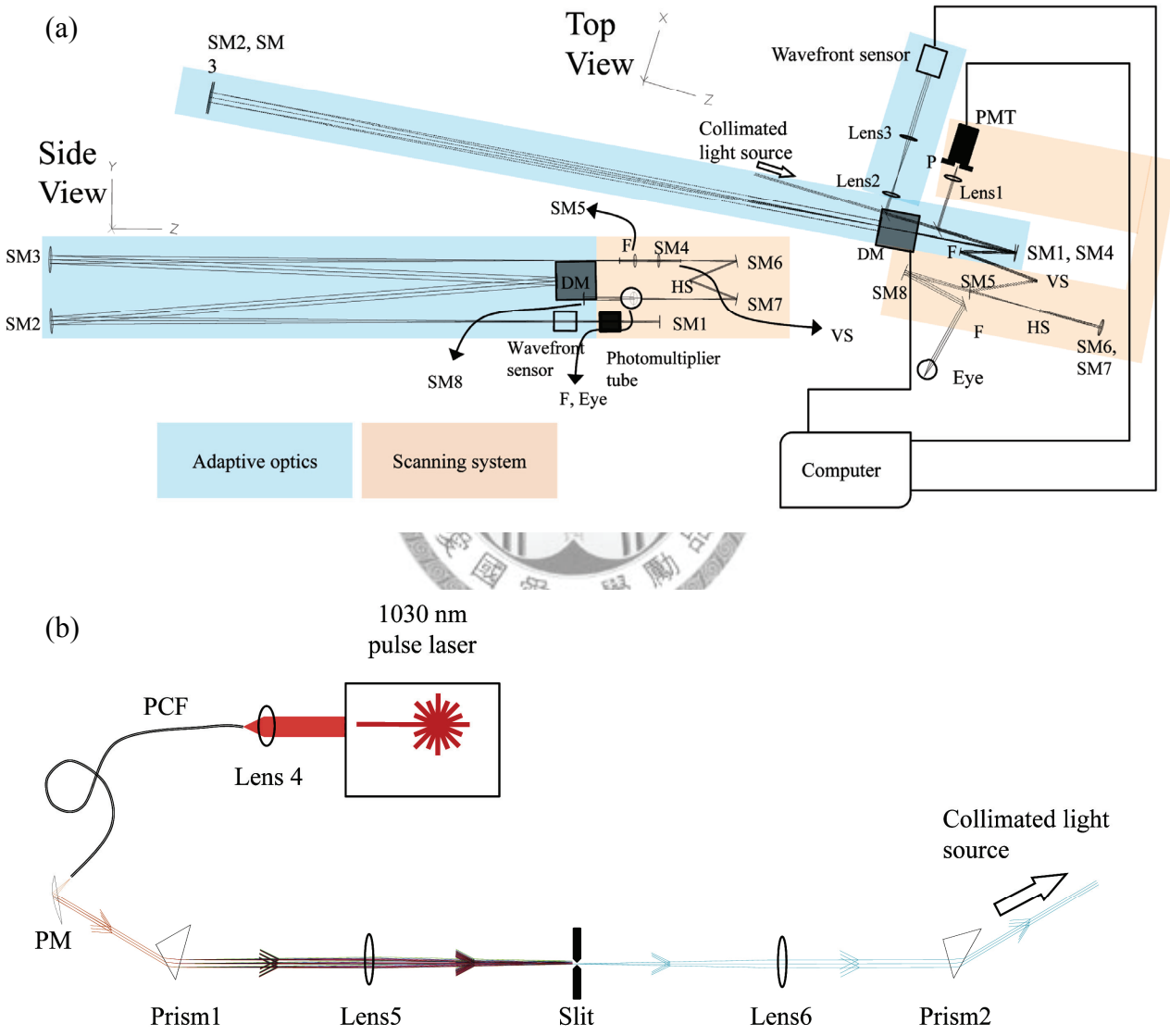


Figure 4.1 The whole system separated into (a) AOSLO and (b) wavelength selector. SMs: spherical mirror; F: flat mirror; DM: deformable mirror; P: pinhole; VS: vertical scanner; HS: horizontal scanner; PMT: photomultiplier tube; PCF: photonic crystal fiber; PM: parabolic mirror. Note that (a) and (b) are in different scale.

## IV.1 Specifications of devices

Laser source and photonic crystal fiber

| | Model number/ *manufacturer* | Description | Notes |
|---|---|---|---|
| Yb:fiber pulse laser | Uranus 005-500-INS/ *PolarOnyx Inc.* | Pulse width: 5 ps.<br>Repetition rate: 50 MHz.<br>Center wavelength: 1030 nm<br>Pulse energy: 10 μJ. | 1030 nm pulse laser |
| Photonic crystal fiber | Custom-made by *Center for Photonics and Photonic Materials, University of Bath* | Pumped by the Yb:fiber pulse laser the wavelength can be extended below 500 nm [17]. | PCF |

Optics

| | Model number/ *manufacturer* | Description | | | Notes |
|---|---|---|---|---|---|
| | | Radius of curvature | Surface coating/ spectral range | Surface accuracy | |
| Spherical mirror | SMCC-1037-0.40-C/ *CVI Technical Optics Ltd.* | 400 mm | EAV/ >90% reflectance within 400~10000 nm | λ /10 | SM1, SM4, SM8 |
| | SMCC-2037-2.00-C/ *CVI Technical Optics Ltd.* | 2000 mm | | λ /10 | SM2,3 |
| | 10DC200/ *Newport Corp.* | 200 mm | AL.2/ >85% reflectance within 400~6000 nm | λ /4 | SM5-7 |
| | | Focal length | | | |
| Plano-convex lens | LA1131-B/ *Thorlabs Inc.* | 50 mm | -B coating/ <1% reflectance within 650~1100 nm | — | Lens2 |
| | LA1608-B/ *Thorlabs Inc.* | 75 mm | | — | Lens3 |
| | LA1986-B/ *Thorlabs Inc.* | 125 mm | | — | Lens5 |
| | KPX097/ *Newport Corp.* | 125 mm | AR.18/ <1% reflectance within 950~1700 nm | λ /4 | Lens6 |
| Beam splitter | BS013/ *Thorlabs Inc.* | — | — | λ /10 | |
| Parabolic mirror | 50328AL/ *Newport Corp.* | 10 mm | Protected Aluminum/ >80% reflectance within 300~10000 nm | — | PM |
| Aspherical Lens | C330TME-B | 3.1 mm | -B coating/ <1% reflectance within 650~1100 nm | — | Lens4 |

Adaptive optics, scanners and the detector

| | Model number/ *manufacturer* | Description | Notes |
|---|---|---|---|
| Wavefront sensor | FrontSurfer Shack-Hartmann Wavefront Sensor-1/ *Flexible Optical B. V.* | Hexagonal 127-microlens array.<br>Aperture: 3.9-mm diameter.<br>Repeatability: λ /300. | Wavefront sensor |
| Deformable mirror | 30mm 37-channel PDM/ *Flexible Optical B. V.* | Number of electrodes: 37<br>Maximum stroke: 8 μm.<br>Aperture: 30-mm diameter. | DM |
| Scanners | PLD-XYG/ *Electro-Optical Products Corp.* | The fast (resonant) and slow (galvo) Scanners are locked in raster scanning mode.<br>Frequency: 16 KHz (fast)/ 28.5 Hz (slow) | HS, VS |
| PMT module | H5783-01/ *Hamamatsu Corp.* | Spectral response: 300~850 nm<br>Anode sensitivity: 30000 A/W<br>Dark current: 4 nA | PMT |

Electronics and software programs

| | Model number/ *manufacturer* | Description | Notes |
|---|---|---|---|
| Computer | — | Mainboard: Asus P5LD2.<br>CPU: Intel Pentium (R) D CPU 3.40 GHz.<br>RAM: 504 MB. | Computer |
| Frame grabber | Alta-AN4/ *BitFlow Inc.* | Analog frame grabber.<br>Max. pixel clock rate: 160 MHz.<br>Video signal voltage: 0~1 V.<br>Frame/line enable: 0~3.5 V TTL. | Installed on computer's mainboard |
| PMT amplifier | C6438-01/ *Hamamatsu Corp.* | Gain: 25 mV/ 1 μA.<br>Gain bandwidth: DC to 50 MHz.<br>Max. output noise: 8 mV. | |
| Video acquisition program | BitFlow SDK 5.00/ *BitFlow Inc.* | — | |
| Adaptive optics program | FrontSurfer 1.3.7.5/ *Flexible Optical B. V.* | — | |
| Optical design program | ZEMAX-EE/ *ZEMAX Development Corp.* | — | |

Opto-mechanics

| | Model number/ *manufacturer* | Description | | | Notes |
|---|---|---|---|---|---|
| | | Dimensions | Resolution | Tunable range | |
| Mount | U100-A3K/ *Newport Corp.* | 1” aperture | 3.8 arc sec | ±7° | |
| | U100-A-LH-3K/ *Newport Corp.* | 1” aperture | 3.8 arc sec | ±7° | |
| | U200-P3K/ *Newport Corp.* | 2” aperture | 2.4 arc sec | ±5° | For SM2,3 |
| | KM100/ *Thorlabs Inc.* | 1” aperture | — | ±4° | |
| | K6X/ *Thorlabs Inc.* | 1” aperture | — | ±4° | For wavefront sensor |
| Stage | 06PTS-0.5M/ *Unice E-O Service Inc.* | 60×60×22 $mm^3$ | 10 μm | 13 mm | For slit |
| | 06TTS-3M/ *Unice E-O Service Inc.* | 114×102×148 $mm^3$ | 100 μm | 60 mm for each axis | For wavefront sensor |
| | 06DTS-3M/ *Unice E-O Service Inc.* | 182×165×194 $mm^3$ | 5 μm | 25 mm for each axis | For confocal pinhole |
| | MDE 122/ *Elliot Scientific Ltd.* | 134×75×66 $mm^3$ | 20 nm | 2 mm for each axis | For PCF coupling |
| Pinhole | P50S/ *Thorlabs Inc.* | 50-μm diameter | 2-μm tolerance | — | P |
| Slit | NT40-488/ *Edmund Optics Inc.* | 56×38×22 $mm^3$ | 10 μm | 0~6.35 mm | Slit |
| Iris | ID25/ Thorlabs Inc. | 43-mm diameter | — | 1~25-mm aperture | |

Table 4.1.1 Part lists. λ here is 633 nm.

## IV.2 Collimated supercontinuum source and wavelength selection

Fig. 4.1 (b) illustrates the idea of separating a narrowband light from a broadband source. After the supercontinuum generation from the PCF we can use a parabolic mirror to obtain collimated beam for without chromatic aberration. This broadband collimated beam is then dispersed by Prism1, and

thus different wavelength has its own direction before entering Lens5. The slight directional difference, after going through Lens5, is transformed to spatial difference on the focal plane of Lens5. The distance between Prism1 and Lens5 is 125 mm, the focal length of Lens5, so that the focused beams of different wavelengths are parallel to each other.

With an adjustable slit on a linear stage on the focal plane of Lens5, we can pick the arbitrary central wavelength (by translating the stage) and bandwidth (by adjusting the slit) out of the original broadband source, as illustrated in fig. 4.2.1.

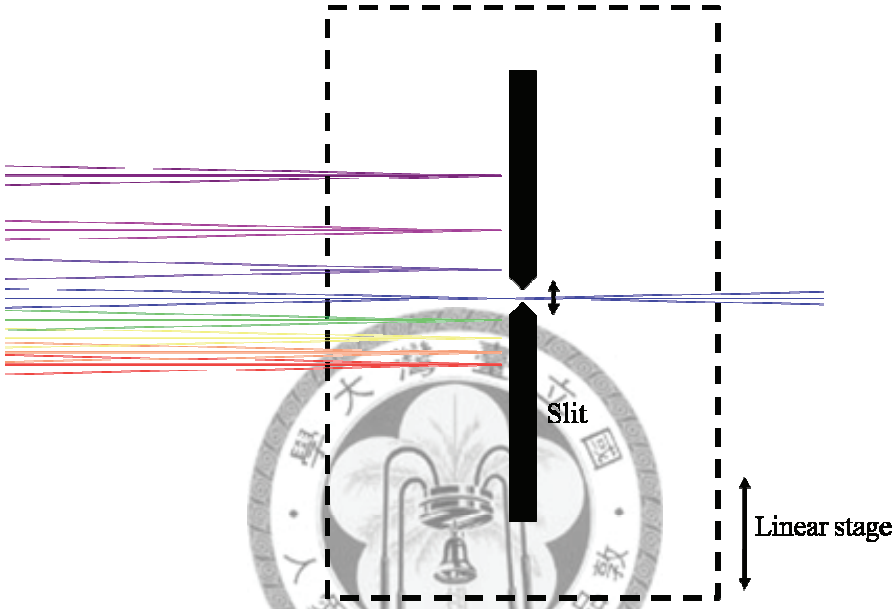


Figure 4.2.1 The enlarged scheme at the focal plane of Lens5.

Lens6 and Prism2 here are adopted to inversely transformed the selected light into collimated beam with fixed output beam path after Prism2. To perform this ability the deployment of Len6 and Prism 2 should be exactly symmetrical to that of Lens5 and Prism1 [35]. In practice Lens6 is installed on a linear stage in order to compensate slight chromatic aberration.

## IV.3 Scanning system

If our construction the optical system relies only on calipers, triangle formula and visual perception, the precision we can achieve would be as large as several tens of micrometers. However, as we

discuss the performance of the system in the previous chapter, the scale of acceptable wavefront error is only one tenth of wavelength, which is tens of nanometers. Therefore, my strategy to overcome this discrepancy is to adopt high-precision adjustable mounts for spherical mirrors. The alignment was first roughly determined by calipers, and then fine tuned with these mirror mounts under the monitoring of the wavefront sensor.

Here I present fig. 4.3.1 instead of all the construction details of these mirrors. The main strategy is using the distance and incident angle between each two mirrors to calculate the distance between their post holders. To determine the angle of incidence possible I projected the beam as far as I can so that the displacement would be measured more precisely. Table 4.3.1 gives the geometry of this scanning system.

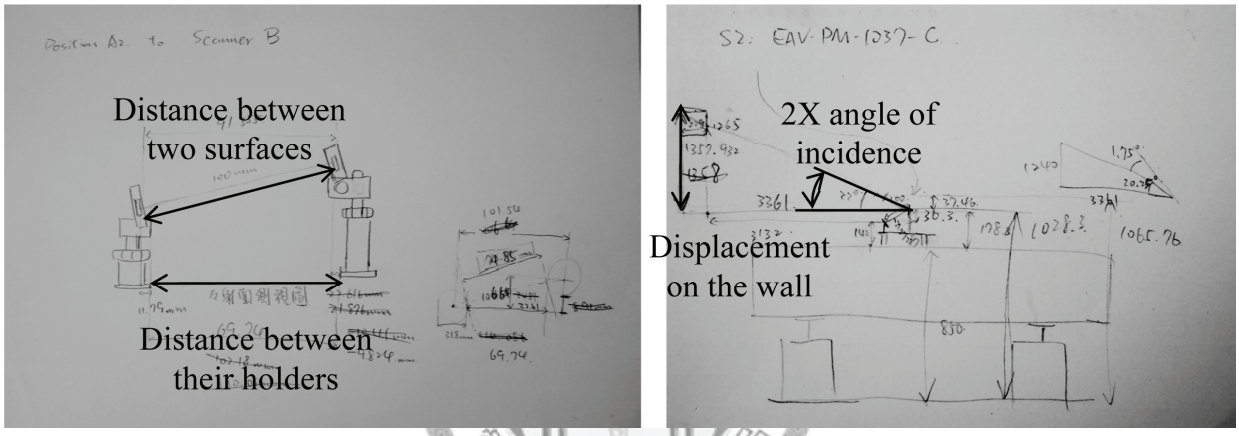


Figure 4.3.1 Calculations during the construction. (a) The distance between two optics. (b) The incident angle on one surface.

| | Description | Radius of curvature (mm) | Aperture size | Distance to next device (mm) | Tilt axis | Incident angle (degree) |
|---|---|---|---|---|---|---|
| HS | Horizontal scanner | Infinity | 4×4 $mm^2$ | 100 | Y | — |
| SM1 | Spherical mirror | 200 | 1” Dia. | 200 | Y | 12.55 |
| SM2 | Spherical mirror | 200 | 1” Dia. | 100 | X | 11 |
| VS | Vertical scanner | Infinity | 5×8 $mm^2$ | 100 | X | 21.64 |
| SM3 | Spherical mirror | 200 | 1” Dia. | 300 | X | 10.64 |
| SM4 | Spherical mirror | 400 | 1” Dia. | — | Y | 6.19 |

Table 4.3.1 Geometry of the scanning system. Refer to fig. 3.2.6 for the denotation here. Dia.: diameter.

## IV.4 Adaptive optics

Apparently an AOSLO is quite large compared with a conventional scanning laser microscope, and the main reason for this hugeness is the adaptive optics. Though these actuators has 8-μm maximum stroke, being capable of compensating peak-to-valley wavefront error up to 15 $\lambda$, it is not possible to pack 37 piezo-based actuators into a 5-mm aperture similar to the beam size. We would need one telescope to magnify the input beam to suit the aperture of the deformable mirror and another telescope to reduce it back.

The two telescopes we used have 5X magnification/ reduction of the beam. The maximum diameters of human eyes are typically 8 mm, but with such a large beam the scanning area would be quite limited, and there are few high-speed resonant scanners fabricated with diameter larger than 5 mm. Therefore we confine the input beam diameter into 4 mm and design the scanning system with 2X magnification. Engineers at OKO have analyzed and demonstrated that the best wavefront correction can be achieved by using only 60% diameter of the DM aperture [36], and thus we adopt 5X-magnification/ reduction telescopes in the adaptive optics design.

Just as the scanning system, the AO system also requires two telescopes, or four spherical mirrors, the aberration compensation technique discussed in III.2 can be applied again. Table 4.4.1 gives the geometry of this AO system.

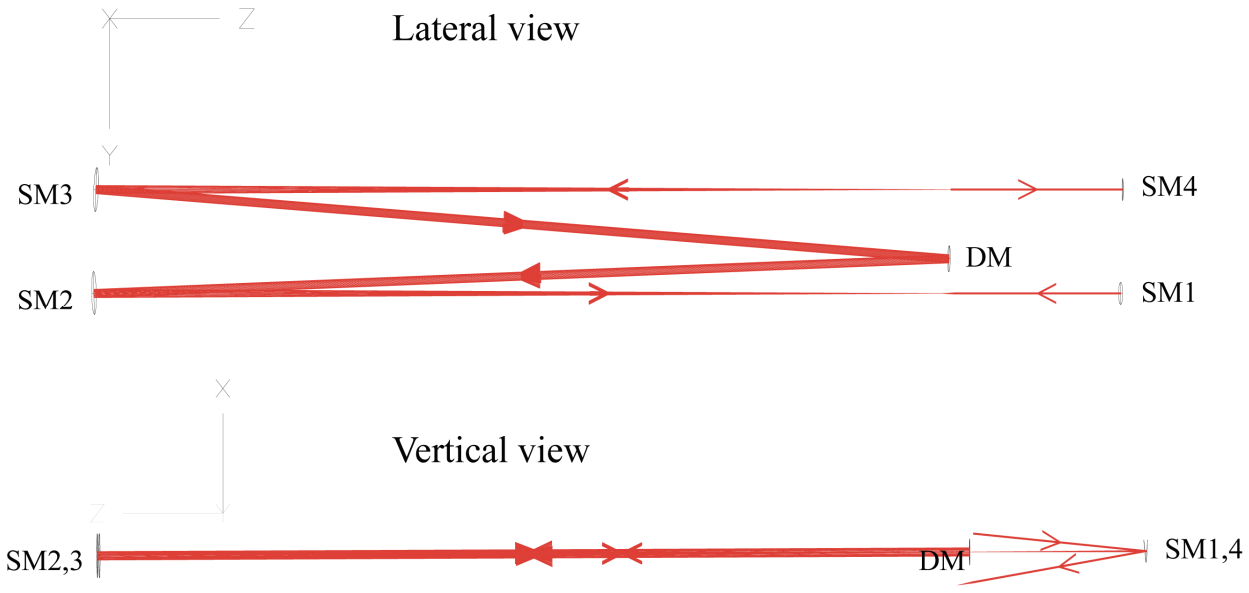


Figure 4.4.1. The AO system.

| | Description | Radius of curvature (mm) | Aperture size | Distance to next device (mm) | Tilt axis | Incident angle (degree) |
|---|---|---|---|---|---|---|
| SM1 | Spherical mirror | 400 | 1” Dia. | 1200 | Y | 3 |
| SM2 | Spherical mirror | 2000 | 2” Dia. | 1000 | X | 2.29 |
| DM | Deformable mirror | Infinity | 30 mm Dia. | 1000 | X | 3.42 |
| SM3 | Spherical mirror | 2000 | 2” Dia. | 1200 | X | 1.14 |
| SM4 | Spherical mirror | 400 | 1” Dia. | — | Y | 5 |

Table 4.4.1. Geometry of the AO system.

## IV.5 Image acquisition

In this section, let us do some back-of-the-envelope calculation on the signal level to verify that the whole electronic system would work properly. The laser power after the supercontinuum generation is far more than enough for our usage, so we should start from considering the safety of the subject's eye.

1. Maximum laser power on human eyes: ~5 μw on the cornea
2. Reflectivity of the retina: ~5%
3. The pupil would block nearly 99% of this reflected light.
4. 13 AL-coated mirrors in the AOSLO: reflectivity ~93% at visible band for each surface.
5. 50:50 beam splitter: ~50% loss.

From these five statements we derive that the residual power to PMT is

$$5\ \mu W \times 0.05 \times 0.01 \times 0.93^{13} \times 0.5 \fallingdotseq 0.0005\ \mu W = 0.5\ nW \qquad \text{Eq. 5.5.1}$$

So far there is 0.5 nW on the PMT, and with a 30000-A/W anode sensitivity we obtain 15-μA current output, which is about 4000 times of the dark current, providing adequate signal-to-noise ratio.

Alta-AN4 accepts only voltage input for video signal, therefore we adopted a 25 mV/μA amplifier to translate the PMT output current into the input voltage of the frame grabber. The 15-μA current is thus amplified to around 400 mV. The maximum gain of Alta-AN4 is 2, which makes the input voltage equivalent to 800 mV. This frame grabber can digitize 0~1-V signal into 16-bit data, and is thus ideal for the signal level of our ophthalmoscope. We synchronize Alta-AN4 with the scanning system through the TTL outputs that E.O.P.C. added for us.

# Chapter V　System performance

Since our ophthalmoscope is developed for high-resolution and hyper-spectral-imaging applications, the performance test will focus on its wavefront flatness and spectral resolution.

## V.1 Spectral resolution

Figure 5.1.1 shows the full width at half maximum (FWHM) of the spectra at different wavelength. As mentioned in IV.2 the width of the slit would decide the bandwidth of the output beam, but this rule is not always true if the width of the slit is as small as the airy diameter. Below the airy diameter there would be no significant reduction of bandwidth but only tremendous power loss. In our case the airy diameter is roughly 40 μm, thus we set the width of the slit 50 μm.

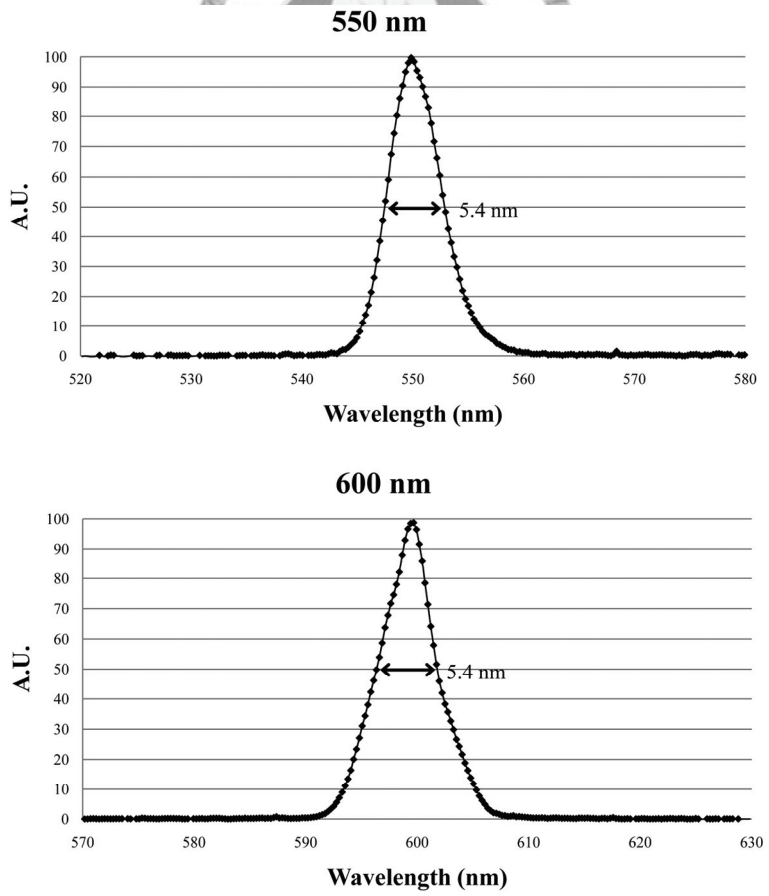

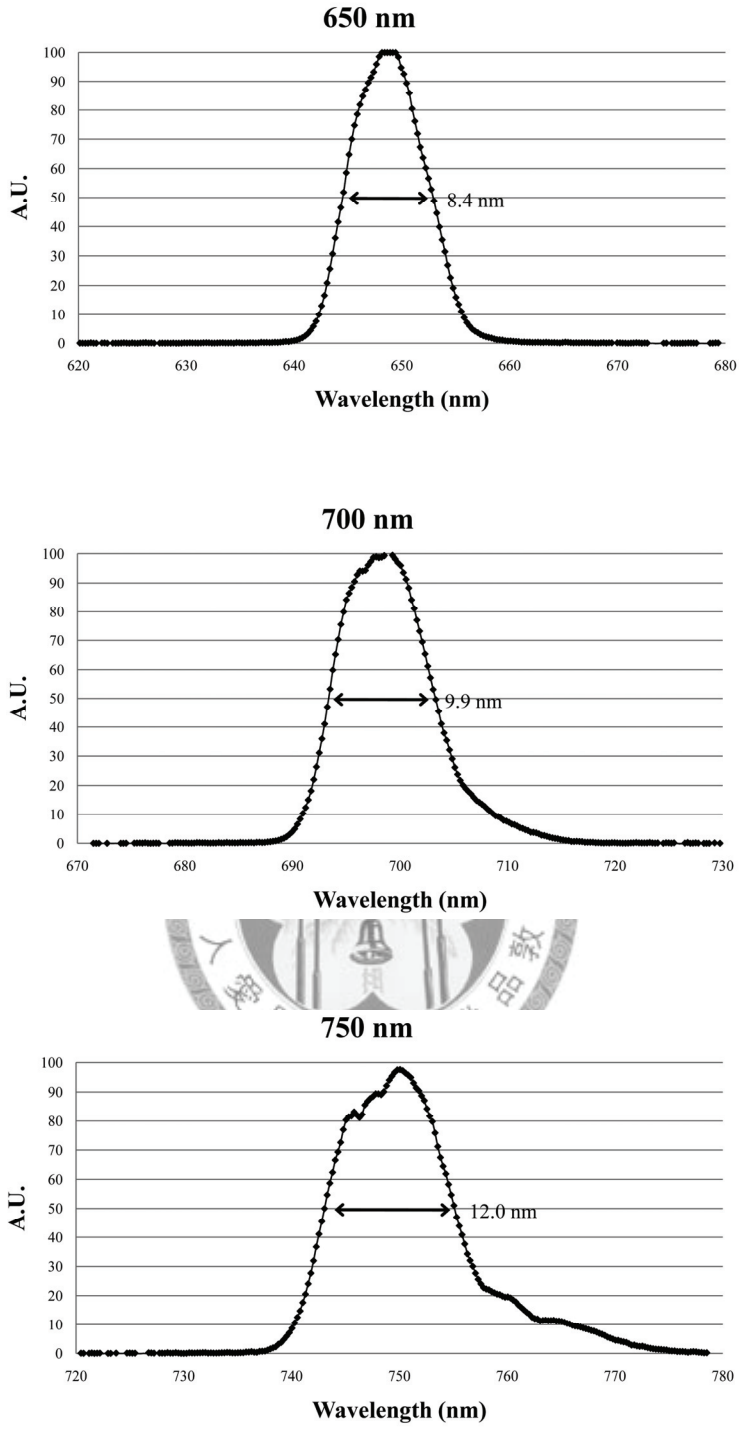


Figure 5.1.1 Spectrographs from the wavelength selector. A.U., arbitrary unit.

Fig. 5.1.1 demonstrates that the spectral resolution we can achieve is roughly 8-nm full-width-half-maximum (FWHM), which means we can divide the visible band up to 40 lines. This resolution decreases as wavelength grows, simply because light of longer wavelength projects larger airy diameter.

## V.2 Wavefront flatness

In chap. III we mainly concentrate on the wavefront flatness at the output end, the pupil of the eye, of the ophthalmoscope. However, we should keep in mind that all these simulations are based on a input beam of ideal-plane-wave propagation mode, and therefore the wavefront quality of the source is critical as well. Fig. 5.2.1 shows the wavefront measurement and corresponding PSF of the output beam of the wavelength selector, from 550-nm to 750-nm wavelength.

**550 nm**

rms wavefront error: 0.030 λ

Peak−to−valley = 0.200 waves
RMS = 0.030 waves
Wavelength = 0.550 mic
Optical power = −0.014 D

Strehl ratio: 0.961

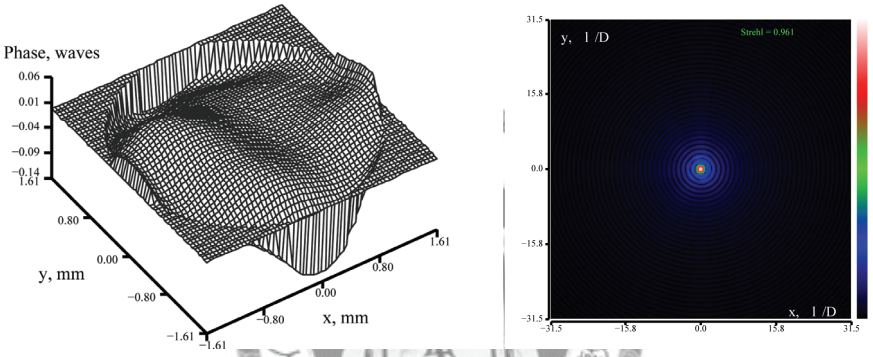


**600 nm**

rms wavefront error: 0.023 λ

Peak−to−valley = 0.132 waves
RMS = 0.023 waves
Wavelength = 0.600 mic
Optical power = −0.017 D

Strehl ratio: 0.984

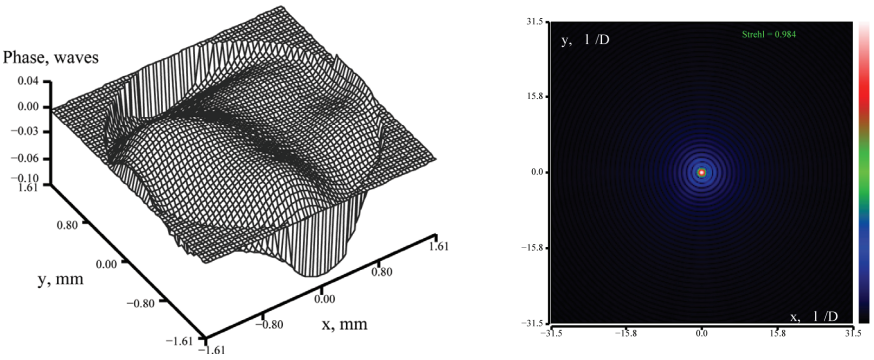

**650 nm**

rms wavefront error: 0.021 λ

Peak−to−valley = 0.122 waves
RMS = 0.021 waves
Wavelength = 0.650 mic
Optical power = −0.014 D

Strehl ratio: 0.983

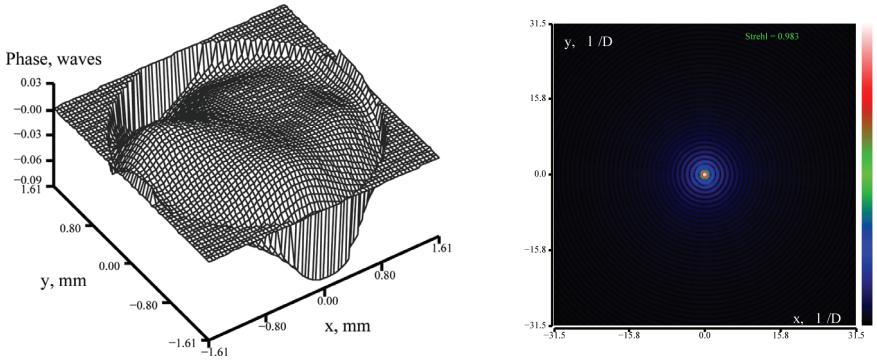


**700 nm**

rms wavefront error: 0.021 λ

Peak−to−valley = 0.106 waves
RMS = 0.021 waves
Wavelength = 0.700 mic
Optical power = −0.013 D

Strehl ratio: 0.985

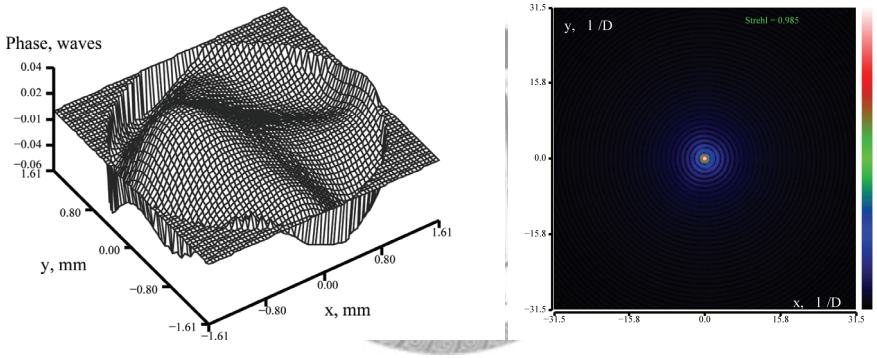


**750 nm**

rms wavefront error: 0.023 λ

Peak−to−valley = 0.107 waves
RMS = 0.023 waves
Wavelength = 0.750 mic
Optical power = −0.016 D

Strehl ratio: 0.981

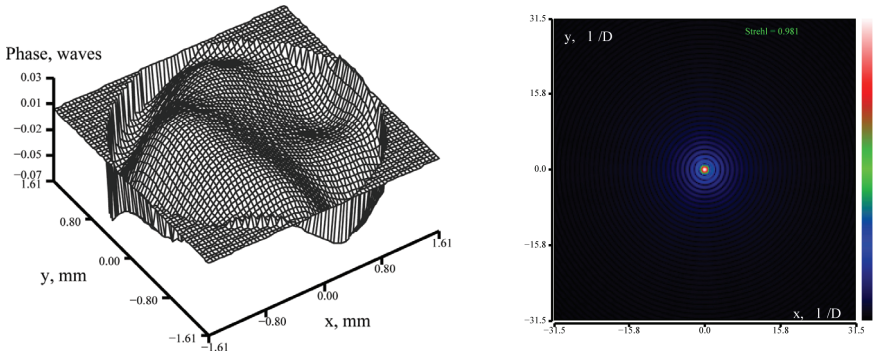


Figure 5.2.1. Wavefront maps and point spread functions of different wavelengths.

Please note that there is indeed certain amount of chromatic aberration resulting from the telescope of the wavelength selector. This amount of chromatic aberration is about 0.5-wave rms wavefront error (mainly defocus) with 25-nm shift in central wavelength. We installed the second lens, Lens6 in fig. 4.1, on a linear stage to compensate this aberration. We recorded that from 550-nm to 750-nm the stage should travel 2.4 mm, and all the measurements presented in fig. 5.2.1 are under chromatic-aberration compensation.

From the measurements above we can be confident of the wavefront flatness of light source, so now we can proceed to measure the wavefront error of the whole AOLSO. As we proposed in the introduction there is not one single lens in the adaptive optics and scanning system, therefore the system is totally free from chromatic aberration after the wavelength selection part. Under this condition the measurement with one fixed wavelength would be adequate to obtain the residual aberration of the system. In fig. 5.2.2 we confirm the diffraction-limited performance of our ophthalmoscope.

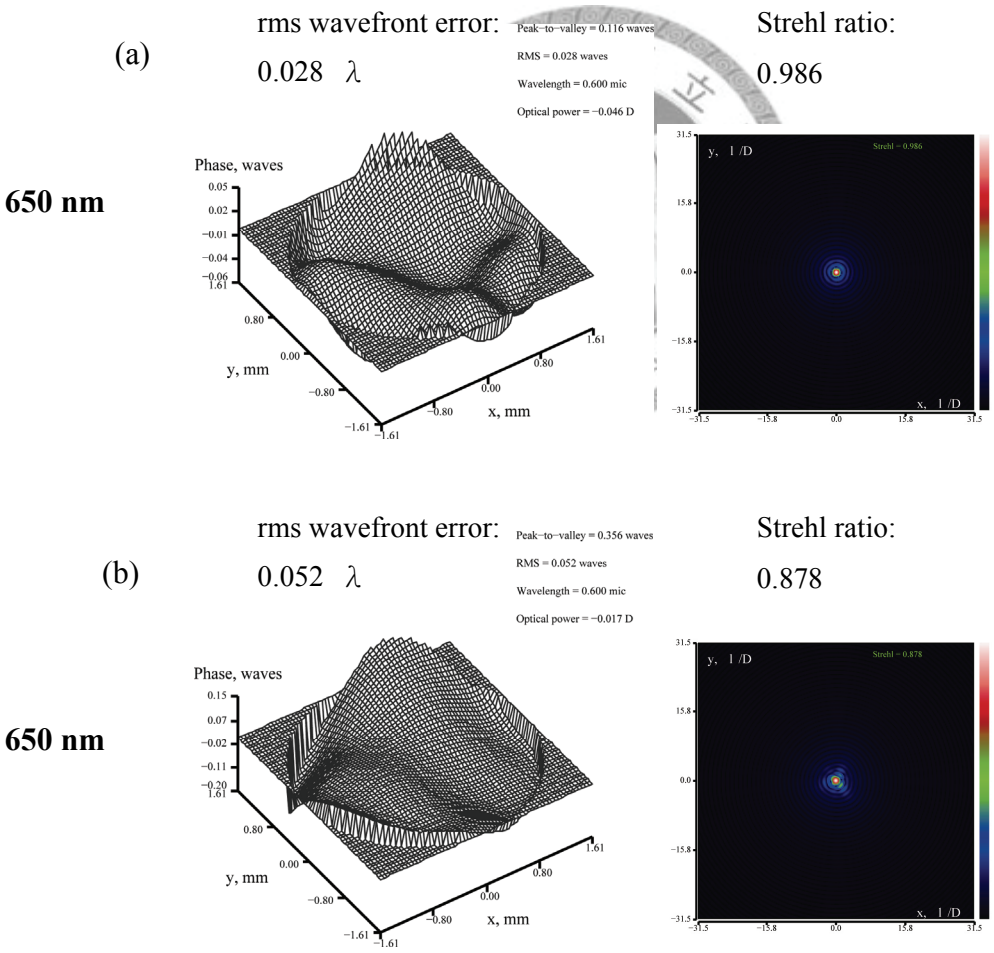


Figure 5.2.2. Wavefront measurements of the whole system. The measurements are (a) at pupil of the eye, and (b) as setup in fig. 4.1 while the eye is replaced with a flat mirror.

# Chapter VI　Discussion and Conclusion

## VI.1 Discussion

Derivations in IV.5 have actually been simplified so the problem of weak signal is not revealed. In fact, reflectivity of the retina from 400-nm to 450-nm wavelength is only 0.1 %, which means the signal level would be two-order smaller than our estimation. This weak signal may be remedied in two ways. First, there are still some PMTs designed with higher anode sensitivity than H5783-01 we used. We can also adopt second-stage amplification in the electronics part.

To realize the function of real-time hyper-spectral imaging, we will to adopt motorized stages for both the slit and Lens6 in the wavelength selector in fig. 4.1 (b). These two stages perform automatic wavelength selection and chromatic aberration compensation, respectively. These two stages are synchronized to the vertical scanner so that the wavelength can be programmed as a function of frame number, and thus we can acquire images of different wavelengths time sequentially. Combining these frames of different wavelengths together a hyper-spectral image is obtained.

## VI.2 Conclusion

In this thesis, we have demonstrated an ophthalmoscope which provides hyper-spectral images with diffraction-limited resolution and 8-nm (averaged) spectral resolution within the visible band. In this system our aberration-compensation design is used for the adaptive optics system and the scanning system. Without inserting any correction optics, our spectro-ophthalmoscope achieves diffraction-limited performance within a 3° ×3° scanning range. The numerical simulation showed us this result is true for all the wavelengths above 532 nm, and we experimentally confirmed it from 550 nm to 750 nm. With a 4-mm beam diameter on the cornea, the lateral resolution approximated by the airy disk formula is roughly 3 μm, fulfilling the subcellular resolution imaging capability. With the aid of adaptive optics the diffraction-limited performance can be expected even the beam diameter is as large as 8 mm [7], and thus the resolution may be improved to 1.5 μm.

Besides the applications in laser scanning ophthalmoscope, this system can be easily modified to various high-resolution scanning laser microscopy with broadband capability, simply substituting a microscope objective for the eye. Since the supercontinuum generation bears the property of pulse laser, and the deformable mirror is in itself a phase modulator, our system can be adopted for

advanced applications such as the nonlinear excitation spectro-microscopy and phase-modulation-related microscopy [37].

# Figure index

# Table index



# Reference


1. C. W. Oyster, *The human eye: structure and function* (Sinauer Associates, Sunderland, Mass., 1999), pp. 470, 562.

2. Medisave, retrieved http://www.medisave.co.uk/welch-allyn-panoptic-ophthalmoscope-p-4469.html.

3. E. Meyer, "Early ophthalmoscope", retrieved http://medschool.umaryland.edu/ophthalmology/History.asp.

4. R. H. Webb, G. W. Hughes, and O. Pomerantzeff, "Flying spot TV ophthalmoscope," Applied Optics **19**(17), 2991-2997 (1980).

5. C. Sheppard and D. Shotton, *Confocal laser scanning microscopy* (BIOS Scientific; Springer in association with the Royal Microscopical Society, 1997), p. 39.

6. D. T. Miller, D. R. Williams, G. M. Morris, and J. Z. Liang, "Images of cone photoreceptors in the living human eye," Vision Research **36**(8), 1067-1079 (1996).

7. J. Z. Liang, D. R. Williams, and D. T. Miller, "Supernormal vision and high-resolution retinal imaging through adaptive optics," Journal of the Optical Society of America A-Optics Image Science and Vision 14(11), 2884-2892 (1997).

8. A. Roorda, F. Romero-Borja, W. J. Donnelly, H. Queener, T. J. Hebert, and M. C. W. Campbell, "Adaptive optics scanning laser ophthalmoscopy," Optics Express **10**(9), 405-412 (2002).

9. J. L. Duncan, Y. H. Zhang, J. Gandhi, C. Nakanishi, M. Othman, K. E. H. Branham, A. Swaroop, and A. Roorda, "High-resolution imaging with adaptive optics in patients with inherited retinal degeneration," Investigative Ophthalmology & Visual Science **48**(7), 3283-3291 (2007).

10. C. H. G. Wirght and S. F. Barrett, "Hybrid retinal photocoagulation system " in Ophthalmic Technologies VII, P. O. Rol, K. M. Joos M.D., and F. Manns, eds. (SPIE, San Jose, 1997), pp.

106-117.

11. S. Stevenson and A. Roorda, "Correcting for miniature eye movements in high resolution scanning laser ophthalmoscopy," in Opthalmic Technologies XV, F. Manns, P. G. Soederberg, A. Ho, B. E. Stuck, and M. Belkin, eds. (SPIE, San Jose, 2005), pp. 145-151.

12. J. I. W. Morgan, A. Dubra, R. Wolfe, W. H. Merigan, and D. R. Williams, “In vivo autofluorescence imaging of the human and macaque retinal pigment epithelial cell mosaic,” Investigate Ophthalmology and Visual Science **50**(3), 1350-1359 (2009).

13. C. Chang, C. Chiao, and H. Y. Yan, “Ontogenetic changes in color vision in the milkfish (Chanos chanos Forsskal, 1775),” Zoological Science **26**(5), 349-355 (2009).

14. K. Grieve, P. Tiruveedhula, Y. H. Zhang, A. Roorda, “Multi-wavelength imaging with the adaptive optics scanning laser ophthalmoscope,” Optics Express **14**(25), 12230-12242 (2006).

15. H. Gross, *Handbook of optical systems* (Wiley-VCH, Weinheim, 2005), Vol. 3, pp. 82-99.

16. H. Gross, *Handbook of optical systems* (Wiley-VCH, Weinheim, 2005), Vol. 1, p. 503.

17. J. M. Stone and J. C. Knight, "Visibly "white" light generation in uniform photonic crystal fiber using a microchip laser," Optics Express **16**(4), 2670-2675 (2008).

18. J. B. Pawley, *Handbook of biological confocal microscopy, 2nd ed.* (Plenum Press, New York, 1990), pp. 167, 212.

19. A. Boyde, "Stereoscopic Images in Confocal (Tandem Scanning) Microscopy," Science **230**(4731), 1270-1272 (1985).

20. G. J. Brakenhoff, H. T. M. Vandervoort, E. A. Vanspronsen, W. A. M. Linnemans, and N. Nanninga, "3-Dimensional chromatin distribution in neuro-blastoma nuclei shown by confocal scanning laser microscopy," Nature **317**(6039), 748-749 (1985).

21. K. Carlsson, P. E. Danielsson, R. Lenz, A. Liljeborg, L. Majlof, and N. Aslund, "3-dimensional microscopy using a confocal laser scanning microscope," Optics Letters **10**(2), 53-55 (1985).

22. N. Streibl, "3-dimensional imaging by a microscope," Journal of the Optical Society of America a-Optics Image Science and Vision **2**(2), 121-127 (1985).

23. R. W. W. Vanresandt, H. J. B. Marsman, R. Kaplan, J. Davoust, E. H. K. Stelzer, and R. Stricker, "Optical fluorescence microscopy in 3 dimensions - microtomoscopy," Journal of Microscopy-Oxford **138**(Apr), 29-34 (1985).

24. T. Wilson, "Scanning optical microscopy," Scanning **7**(2), 79-87 (1985).

25. T. Wilson and A. R. Carlini, "Size of the detector in confocal imaging-systems," Optics Letters **12**(4), 227-229 (1987).

26. H. W. Babcock, "The possibility of compensating astronomical seeing," Publication of the astronomical society of the pacific **65**(386), 229-236 (1953).

27. J. W. Hardy, J. E. Lefebvre, and C. L. Koliopoulos, "Real-time atmospheric compensation," Journal of the Optical Society of America **67**(3), 360-369 (1977).

28. C. E. Max, G. Canalizo, B. A. Macintosh, L. Raschke, D. Whysong, R. Antonucci, and G. Schneider, "The core of NGC 6240 from Keck adaptive optics and Hubble Space Telescope NICMOS observations," Astrophysical Journal **621**(2), 738-749 (2005).

29. M. S. Smirnov, “Measurement of wave aberration in human eye,” Biophysics-USSR **6**(6), 52-& (1961).

30. F. Berny and S. Slansky, *Optical instruments and techniques*, H. Dickson, ed. (Oriel, London, 1970), pp. 375-386.

31. G. Walsh, W. N. Charman, and H. Howland, “Objective technique for the determination of monochromatic aberrations of the human-eye,” Journal of the Optical Society of America A-Optics Image Science and Vision **1**(9), 987-992 (1984).

32. J. Z. Liang, B. Grimm, S. Goelzs, and J. F. Bille, “Objective measurement of wave aberrations of the human eye with the use of a Hartmann-Shack wave-front sensor,” Journal of the Optical Society of America A-Optics Image Science and Vision **11**(7), 1947-1957 (1994).

33. S. A. Burns, R. Tumbar, A. E. Elsner, D. Ferguson, and D. X. Hammer, "Large-field-of-view, modular, stabilized, adaptive-optics-based scanning laser ophthalmoscope," Journal of the Optical Society of America a-Optics Image Science and Vision **24**(5), 1313-1326 (2007).

34. D. C. Hanna, "Astigmatic Gaussian beams produced by axially asymmetric laser cavities," Ieee Journal of Quantum Electronics Qe **5**(10), 483-& (1969).

35. D. Wildanger, E. Rittweger, L. Kastrup, and S. W. Hell, "STED microscopy with a supercontinuum laser source," Optics Express **16**(13), 9614-9621 (2008).

36. G. Vdovin, O. Soloviev, A. Samokhin, and M. Loktev, "Correction of low order aberrations using continuous deformable mirrors," Optics Express **16**(5), 2859-2866 (2008).

37. A. Leray, K. Lillis, and J. Mertz, "Enhanced background rejection in thick tissue with differential-aberration two-photon microscopy," Biophysical Journal **94**(4), 1449-1458 (2008).